Endocytosis is required for access of surface-bound cargo to the flagellar pocket of trypanosomes

Running title: Characterisation of TbSmee1 (27)

Authors:
Daja Schichler[1], Eva-Maria Spath*[2], Antonia Konle*, Sina Riegler*, Alexandra Klein°, Anna Seleznev°, Sisco Jung°, Tim Wuppermann#, Noah Wetterich#, Alyssa Borges, Elisabeth Meyer-Natus, Katharina Havlicek[3], Sonia Pérez Cabrera[4], Korbinian Niedermüller, Sara Sajko[5], Maximilian Dohn, Xenia Malzer, Emily Riemer, Tuguldur Tumurbaatar, Kristina Djinovic-Carugo[5,6], Gang Dong[7], Christian J. Janzen, Brooke Morriswood.

*/°/# These authors contributed equally

Affiliations:
Unless stated otherwise: Department of Cell & Developmental Biology, Biocenter, University of Würzburg, Würzburg, Germany

1 present address: Cell Biology and Biophysics Unit, EMBL, Heidelberg, Germany
2 present address: Department of Internal Medicine 1, Friedrich-Alexander-University Erlangen-Nuremberg, Erlangen, Germany
3 Department of Biochemistry and Cell Biology, Max Perutz Labs, University of Vienna, Vienna Biocenter (VBC) Vienna, Austria
4 Francisco de Vitoria University, Madrid, Spain
5 Department of Structural and Computational Biology, Max Perutz Labs, University of Vienna, Vienna Biocenter (VBC), Vienna, Austria
6 Department of Biochemistry, Faculty of Chemistry and Chemical Technology, University of Ljubljana, Ljubljana, Slovenia
7 Center for Medical Biochemistry, Max Perutz Labs, Medical University of Vienna, Vienna Biocenter (VBC) Vienna, Austria

Email for correspondence: brooke.morriswood@uni-wuerzburg.de

Keywords: Trypanosoma brucei, cytoskeleton, hook complex, TbSmee1, flagellar pocket

Summary: Characterisation of the essential trypanosome protein TbSmee1 suggests that endocytosis is required for flagellar pocket access of surface-bound cargo

Abstract

All endo- and exocytosis in the African trypanosome *Trypanosoma brucei* occurs at a single subdomain of the plasma membrane. This subdomain, the flagellar pocket, is a small vase-shaped invagination containing the root of the cell's single flagellum. Several cytoskeleton-associated multiprotein complexes are coiled around the neck of the flagellar pocket on its cytoplasmic face. One of these, the hook complex, may affect macromolecule entry into the flagellar pocket lumen. In previous work, knockdown of the hook complex component TbMORN1 resulted in larger cargo being unable to enter the flagellar pocket. In this study, the hook complex component TbSmee1 was characterised in bloodstream form *Trypanosoma brucei* and was found to be essential for cell viability. TbSmee1 knockdown resulted in flagellar pocket enlargement, and impaired access to the pocket membrane by surface-bound cargo. Inhibition of endocytosis by knockdown of clathrin phenocopied TbSmee1 knockdown, suggesting that endocytic activity itself is a prerequisite for the entry of surface-bound cargo into the flagellar pocket.

Introduction

The flagellated parasitic protist *Trypanosoma brucei* lives in the bloodstream of its mammalian hosts, in continuous exposure to the immune system. Endo- and exocytosis are therefore critical to the parasite's survival, as they are used to remove bound antibodies from the cell surface and scavenge macromolecular nutrients from the surroundings (Borst and Fairlamb, 1998; Engstler et al., 2007). Remarkably, all endo- and exocytosis in *T. brucei* occurs at just a single subdomain of the plasma membrane, despite the overall rate of endocytosis being comparable to a professional phagocyte (Engstler et al., 2004; Grunfelder et al., 2003). This subdomain is a small vase-shaped invagination that houses the root of the cell's single flagellum. It is called the flagellar pocket (Halliday et al., 2021; Lacomble et al., 2009).

Fluid-phase or surface-bound cargo entering the flagellar pocket is rapidly internalised by clathrin-mediated endocytosis, and then routed to the endosomal/lysosomal system (Link et al., 2021; Overath and Engstler, 2004). Depletion of clathrin results in a gross enlargement of the flagellar pocket due to an imbalance between endocytosis and exocytosis, and causes cargo accumulation inside the flagellar pocket (Allen et al., 2003). Although endocytosis in *T. brucei* is relatively well-characterised, the exact mechanism(s) by which fluid-phase and surface-bound cargo enter the flagellar pocket is less well-understood.

Coiled around the neck of the flagellar pocket on its cytoplasmic face are a number of poorly-characterised cytoskeleton-associated complexes, which might contribute to these processes

75 (Esson et al., 2012; Halliday et al., 2019). The flagellar pocket collar demarcates the boundary
76 between the flagellar pocket and the flagellar pocket neck, and contains the protein TbBILBO1
77 (Bonhivers et al., 2008; Florimond et al., 2015). The centrin arm is a centrin-containing kinked
78 rod which appears to be involved in the biogenesis of various cytoskeleton-associated
79 structures (Selvapandiyan et al., 2007; Shi et al., 2008). The hook complex is a hook-shaped
80 multiprotein complex that sits atop the flagellar pocket collar and alongside the centrin arm. It
81 contains the protein TbMORN1 (Morriswood et al., 2009). Previous characterisation of
82 TbMORN1 revealed that it is essential for the viability of bloodstream form *T. brucei* cells
83 (Morriswood and Schmidt, 2015). Cells depleted of TbMORN1 have enlarged flagellar
84 pockets, indicative of an endocytosis defect. In addition, although small endocytic reporters
85 were still capable of entering the enlarged flagellar pocket, the access of larger
86 macromolecules such as the lectin concanavalin A (ConA) or bovine serum albumin (BSA)
87 conjugated to 5 nm gold particles was blocked. On this basis, it was proposed that the hook
88 complex might be regulating the passage of large macromolecules through the flagellar pocket
89 neck, and thereby mediating cargo entry into the flagellar pocket.
90
91 In this study, the hook complex protein TbSmee1 was characterised in bloodstream form *T.*
92 *brucei*. TbSmee1 (Tb927.10.8820) was initially identified in a proximity labelling screen using
93 TbMORN1 as bait, and shown to localise to the shank part of the hook complex (Morriswood
94 et al., 2013). It was subsequently characterised in procyclic form *T. brucei*, the life cycle stage
95 found within the tsetse fly vector (Perry et al., 2018). In bloodstream form *T. brucei,* depletion
96 of TbSmee1 phenocopies TbMORN1, with ConA and BSA unable to access an enlarged
97 flagellar pocket. Surprisingly, clathrin-depleted cells also exhibited this flagellar pocket access
98 phenotype, suggesting that endocytosis is required for the entry of surface-bound cargo into
99 the flagellar pocket.
100
101
102 **Results**
103 **TbSmee1 is a cytoskeleton-associated phosphoprotein.**
104 Bioinformatic analysis predicted that TbSmee1 is composed of three structured domains
105 separated by linker regions (Fig. 1A). Specifically, a multiple sequence alignment of the
106 TbSmee1 protein with orthologues from other trypanosome species indicated the presence of
107 three blocks of highly-conserved sequence (Fig. S1). These blocks of conserved sequence
108 also corresponded to regions of predicted secondary structure (Fig. S2).
109
110 Two polyclonal antibodies (303, 304) were raised against a recombinant TbSmee1(1-400)
111 truncation, and a third (508) was raised against two peptides (Fig. 1A, green lines). The

112 specificity of the antibodies was confirmed using immunoblots of whole-cell lysates obtained
113 from TbSmee1 RNAi cells and 3xTy1-TbSmee1 endogenous replacement cells. In situ tagging
114 of the *SMEE1* gene in the 3xTy1-TbSmee1 cells was confirmed by PCR analysis of genomic
115 DNA (Fig. S3A,B). All three antibodies detected a band of ~ 85 kDa in the immunoblots, which
116 was strongly depleted in the RNAi (Tet +) samples (Fig. 1B, upper panels. An extra band
117 corresponding to 3xTy1-TbSmee1 was seen in lysates from the endogenous replacement
118 (End. repl.) cells). This extra band was also detected using anti-Ty1 antibodies, confirming its
119 identity (Fig 1B, lower panels).
120
121 To investigate TbSmee1 association with the cytoskeleton, cells were fractionated using
122 nonionic detergent (Fig. 1C). TbSmee1 co-fractionated with the cytoskeleton markers PFR1,2,
123 confirming that it was cytoskeleton-associated (Fig. 1D). Interestingly, the fuzzy appearance
124 of the TbSmee1 band observed in immunoblots of whole-cell lysates was reduced or absent
125 in the fractionation blots (compare Fig. 1B and Fig. 1D). TbSmee1 is heavily phosphorylated
126 in vivo, and is a substrate and potential binding partner of the mitotic kinase TbPLK (Benz and
127 Urbaniak, 2019; McAllaster et al., 2015). The existence of different phosphoforms of a protein
128 is known to cause a fuzzy appearance of bands in gels, so one explanation for this was that
129 exposure of TbSmee1 to endogenous phosphatases during the extraction step was causing
130 dephosphorylation.
131
132 To investigate whether the band collapse could be attributed to dephosphorylation of
133 TbSmee1, extracted cytoskeletons were incubated with exogenous phosphatase at various
134 timepoints prior to immunoblotting. Incubation with exogenous phosphatase resulted in a
135 progressive collapse of the TbSmee1 band over a 20 min period (Fig. 1E). This band collapse
136 was not seen when the samples were in the presence of phosphatase inhibitors either at RT
137 or on ice, or kept on ice (Fig. 1E, last three lanes). The fuzzy appearance of TbSmee1 in
138 immunoblots could therefore be attributed exclusively to phosphorylation.
139
140
141 **TbSmee1 localises to the shank part of the hook complex.**
142 The localisation of endogenous and tagged TbSmee1 protein was analysed in bloodstream
143 form *T. brucei* cells using immunofluorescence microscopy (Fig. 1F). All three main stages of
144 the cell division cycle (1K1N, 2K1N, 2K2N) were analysed. In 1K1N cells (i.e. those with a
145 single kinetoplast, K, and nucleus, N), TbSmee1 localised to a single structure near the
146 flagellum base, consistent with the position of the hook complex (Fig. 1F, arrow). Interestingly,
147 in 2K1N and 2K2N cells there was a third subpopulation of TbSmee1 at varying distances
148 along the cell body in addition to the replicated hook complex (Fig. 1F, arrowheads). This

149 subpopulation was fainter in 2K2N cells than 2K1N ones. The same TbSmee1 distributions
150 were seen using all three anti-TbSmee1 antibodies, and also with anti-Ty1 antibodies in
151 3xTy1-TbSmee1 cells (Fig. S3C). In the endogenous replacement cells, the anti-TbSmee1
152 and anti-Ty1 signals colocalised (Fig. S3D).
153
154 To confirm the localisaiton of TbSmee1 at the hook complex, colabelling experiments were
155 carried out. As expected, TbSmee1 strongly overlapped with the shank part of the hook
156 complex as labelled by TbMORN1 and TbLRRP1 (Fig. 2A,B). The signals were strongly
157 correlated (graphs at right). TbSmee1 also strongly overlapped with the hook complex protein
158 Tb927.10.3010. This 133 kDa protein was one of the top hits in the BioID screen using
159 TbMORN1 (Morriswood et al., 2013). Consistent with the convention started with TbSmee1,
160 Tb927.10.3010 was named TbStarkey1 after another one of Captain Hook's pirates. Two anti-
161 peptide antibodies were generated against TbStarkey1, and their specificity was confirmed by
162 immunoblotting and immunofluorescence imaging of TbStarkey1 RNAi cells (Fig. S4A,B).
163 Strong overlap seen between TbSmee1 and TbStarkey1 was seen on the shank part of the
164 hook complex, and the signals were again strongly correlated (Fig. S4C).
165
166 As expected, TbSmee1 showed only a partial overlap with TbCentrin4, a marker of the centrin
167 arm, and little overlap with TbBILBO1, a marker of the flagellar pocket collar (Fig. 2C, D).
168 Despite the low level of co-occurrence between TbSmee1, TbCentrin4, and TbBILBO1, the
169 signals were strongly correlated. The high levels of global correlation even when the level of
170 co-occurrence was low probably reflects the fact that all these structures are closely
171 juxtaposed in a small volume of intracellular space. In summary, TbSmee1 was localised to
172 the shank part of the hook complex, and showed strong correlation with both strongly and
173 partially overlapping markers (Fig. 2E).
174
175
176 **TbSmee1 is transiently associated with the flagellum attachment zone (FAZ) tip.**
177 The flagellum attachment zone (FAZ) is a cytoskeleton-associated apparatus that adheres the
178 flagellum of *T. brucei* to the cell body (Sunter and Gull, 2016). During replication, a new FAZ
179 is assembled and grows from its initiation point very close to the hook complex towards the
180 anterior end of the cell (Sunter et al., 2015; Zhou et al., 2015). It was previously shown that a
181 tagged version of TbSmee1 is transiently localised to the tip of the new FAZ in replicating
182 insect-stage *T. brucei* cells, in addition to its hook complex localisation (Perry et al., 2018).
183 This dynamic localisation contrasts with other hook complex proteins such as TbMORN1,
184 which are localised exclusively to the hook complex.
185

186 To investigate whether the endogenous TbSmee1 subpopulation seen in 2K1N and 2K2N
187 BSF cells corresponded to the FAZ tip, TbSmee1 and the FAZ marker FAZ1 were analysed
188 at different stages of the cell division cycle. As expected, the TbSmee1 present at the hook
189 complex showed a partial overlap with the posterior end of the FAZ (Fig. 3A, arrow). The extra
190 TbSmee1 subpopulation in 2K1N and 2K2N cells overlapped with the tip of the new FAZ (Fig.
191 3A, arrowheads). The TbSmee1 signal got fainter as the new FAZ elongated, and was quite
192 faint in the 2K2N stage. TbSmee1 was sometimes faintly observed along the full length of the
193 new FAZ in replicating cells, and upon careful observation, a TbSmee1 signal could also be
194 detected at the tip of the old FAZ as well, even in 1K1N cells.
195
196 Using structured illumination microscopy, TbSmee1 was observed to be slightly in front of the
197 tip of the new FAZ filament (Fig. 3B). This suggested that TbSmee1 might be present at the
198 "groove". The groove is a structure involved in remodelling of the microtubule cytoskeleton
199 during cell replication in bloodstream form *T. brucei* (Hughes et al., 2013). It can be detected
200 using the monoclonal antibody DOT1. TbSmee1 appeared to be just behind and slightly
201 enveloped by the DOT1 labelling, confirming its presence at the groove (Fig. 3C). In summary,
202 in replicating cells TbSmee1 is present at the groove in addition to the hook complex, and
203 travels in front of the newly-assembling FAZ filament.
204
205
206
207 **The C-terminal part of TbSmee1 is required for targeting to the hook complex.**
208 To determine what parts of TbSmee1 primary structure are responsible for targeting to the
209 hook complex, a series of truncation constructs based on the predicted domain architecture
210 of TbSmee1 were designed (Fig. 4A). Cell lines that could inducibly express each of these
211 truncations with an N-terminal Ty1 tag were generated. The presence of the ectopic
212 transgenes in the genomes of these cells was confirmed by PCR analysis of genomic DNA
213 (Fig. S5A). To determine the localisation of each construct, and whether it could associate
214 with the cytoskeleton, detergent-extracted cells were analysed using immunofluroescence
215 microscopy.
216
217 TbSmee1(161-766) correctly localised to the hook complex, indicating that Domain1 is not
218 necessary for targeting (Fig. 4B). TbSmee1(265-766) also localised correctly, indicating that
219 the predicted linker region between Domain1 and Domain2 is not necessary for localisation
220 (Fig. 4B). No other truncations were observed to localise to the hook complex, making
221 TbSmee1(265-766) the smallest construct to localise correctly. Expression of all TbSmee1
222 truncations was confirmed by immunoblotting with anti-TbSmee1 and anti-Ty1 antibodies

223 (Figs 4C, S5A). Quantification of the immunoblots indicated that most were expressed at
224 around the level of the endogenous protein (Fig. 4D).
225
226 Interestingly, TbSmee1(161-766) also localised to the FAZ tip in replicating cells (Fig. S5B).
227 TbSmee1(265-766) did not localise to the FAZ tip, suggesting that the linker region between
228 domain1 and Domain2 (aa 161-264) might mediate targeting to this structure. In support of
229 this hypothesis, TbSmee1(2-400) was found to localise to the FAZ tip despite not localising to
230 the hook complex (FigS5C).
231
232
233 **TbSmee1 is essential for the viability of BSF *T. brucei*, and its depletion causes gross**
234 **enlargement of the flagellar pocket.**
235 The effects of TbSmee1 depletion were analysed using tetracycline-inducible RNAi. Induction
236 of RNAi (Tet+) resulted in a rapid cessation of population growth after around 24 h (Fig. 5A).
237 Visual inspection of the stalled populations at 48 h and 72 h post-induction showed widespread
238 lysis, confirming that TbSmee1 is essential for the viability of bloodstream form cells in vitro.
239 A shorter timecourse with higher sampling frequency indicated that the growth defect began
240 after around 20 h of RNAi, and was already clear at 24 h (Fig. 5A, inset).
241
242 TbSmee1 depletion was confirmed at the single-cell level using immunofluorescence
243 microscopy (Fig. 5B). TbSmee1 signal was lost from both the hook complex and FAZ tip. The
244 kinetics of TbSmee1 protein depletion either side of the onset of the growth defect were
245 assessed by immunoblotting. TbSmee1 protein levels were reduced to ~ 20-25% at 15 h and
246 18 h post-induction, with a further reduction to around 10-15% from 21 h onwards (Fig. 5C).
247
248 The effect of TbSmee1 knockdown on cell cycle progression was assessed by quantifying the
249 numbers of 1K1N, 2K1N, 2K2N, and abnormal cell types in the same time window (Fig. S6A).
250 An increase in 2K1N and a decrease in 1K1N cells was visible from 21 h post-induction
251 onwards, followed by an increase in 2K2N cells at the 24 h timepoint. This indicated that cell
252 cycle progression was inhibited from around 21 h after induction of RNAi, correlating with the
253 onset of the growth defect. To summarise, TbSmee1 protein was already significantly depleted
254 at 15 h, with subsequent effects on population growth and cell cycle progression visible from
255 around 21 h onwards.
256
257 The effects of TbSmee1 depletion on other hook complex proteins and also components of
258 the centrin arm and flagellar pocket collar were systematically evaluated (Fig. S7A-E).
259 TbSmee1 depletion resulted in a weak effect on TbLRRP1 (Fig. S7C), but no other structural

260 consequences were observed. Conversely, depletion of TbMORN1 resulted in reductions in
261 the levels of TbSmee1, TbStarkey1, and potentially also TbLRRP1 (Fig. S7A, F-H). The lack
262 of observed structural changes to the hook complex, flagellar pocket collar, and centrin arm
263 following TbSmee1 depletion implied that the lethal phenotype might be due to a loss of
264 function.
265
266 The most obvious morphological effect of TbSmee1 depletion was the gradual accumulation
267 of cells with enlarged flagellar pockets (Fig. 5D). Interestingly, depletion of TbStarkey1 also
268 frequently resulted in the generation of cells with enlarged flagellar pockets, despite causing
269 no growth defect (Fig. S6B-D). This means that depletion of three separate hook complex
270 proteins - TbMORN1, TbSmee1, TbStarkey1 - results in flagellar pocket enlargement, though
271 with varying magnitudes of effect.
272
273
274 **Flagellar pocket enlargement is an early consequence of TbSmee1 depletion.**
275 Flagellar pocket enlargement is not an uncommon phenotype in bloodstream form RNAi cells,
276 and can be both a direct or an indirect consequence of protein depletion (Ali et al., 2014; Allen
277 et al., 2003; Hall et al., 2004; Hall et al., 2005; Price et al., 2007).
278
279 To determine whether flagellar pocket enlargement was an early (and therefore probably
280 direct) consequence of TbSmee1 depletion, a fluorescent, fixable 10 kDa dextran reporter was
281 used. Dextran is a polysaccharide that traffics in the fluid phase and is well-established as an
282 endocytic marker. Control (-Tet) and TbSmee1-depleted (+Tet) cells were incubated on ice in
283 order to block endocytosis (Brickman et al., 1995). The cells were then incubated with the
284 labelled dextran for 15 min to allow it to enter the flagellar pocket, and then fixed afterwards
285 (Fig. 6A). The magnitude of the dextran signal should therefore be proportional to flagellar
286 pocket volume. Visual analysis of the cells confirmed that dextran visibly labelled the flagellar
287 pocket, with a much greater signal seen for cells with an enlarged flagellar pocket (Fig. 6B).
288
289 Flow cytometry was then used for high-throughput, unbiased, and quantitative analysis of the
290 cells (Fig. 6C). At 15 h post-induction, no difference between TbSmee1-depleted cells and
291 controls was observed. At 18 h and 21 h post-induction a slight "shoulder" on the +Tet traces
292 became visible, indicating the emergence of cells with higher fluorescence values than seen
293 in controls. By 24 h post-induction there was a clear hump visible in the traces, indicating a
294 subpopulation with fluorescence values sometimes two orders of magnitude greater than
295 those seen in control cells (Fig. 6C, arrow). Quantification of the flow cytometry data from
296 multiple experiments showed that average fluorescence intensity of the whole + Tet population

297 was noticeably higher than controls at 21 h and 24 h post-induction (Fig. 6D). Even at 18 h
298 post-induction, i.e. before the onset of the growth defect, there was already a clear increase
299 in the average fluorescence intensity in the + Tet population (Fig. 6D, blue arrow). This strongly
300 suggests that flagellar pocket enlargement is an early and probably direct consequence of
301 TbSmee1 depletion.
302
303
304 **TbSmee1 depletion results in impaired flagellar pocket access of surface-bound cargo.**
305 It was previously shown that the ability of large cargo to enter the flagellar pocket is affected
306 after knockdown of the hook complex protein TbMORN1 (Morriswood and Schmidt, 2015).
307 Specifically, the fluid phase marker 10 kDa dextran accumulates in the enlarged flagellar
308 pocket of TbMORN1-depleted cells, while larger fluid phase cargo such as BSA-5 nm gold
309 and large surface-bound cargo such as ConA (which binds to surface glycoproteins) do not
310 access the flagellar pocket lumen.
311
312 To test whether TbSmee1 knockdown also impairs flagellar pocket access, TbSmee1 RNAi
313 cells were incubated with both dextran and ConA to simultaneously monitor the uptake of fluid
314 phase and surface-bound cargo. The cells were first incubated on ice to block endocytosis,
315 and then with the reporters (also on ice) to allow ConA to bind and dextran to enter the flagellar
316 pocket. The cells were then shifted to 37ºC to reactivate endocytosis, and subsequently fixed
317 and imaged (Fig. 7A).
318
319 In control cells, both dextran and ConA were observed to strongly overlap in the part of the
320 cell corresponding to the endosomal/lysosomal system (Fig. 7B, -Tet, arrow). To confirm that
321 the internalised material was being trafficked to the lysosome, the cells were labelled with
322 antibodies specific for the lysosomal enzyme p67 (Kelley et al., 1999). The dextran reporter
323 was not compatible with immunolabelling, but the ConA signal clearly overlapped with the
324 lysosome marker p67 (Fig. S8, -Tet cells). In TbSmee1-depleted cells, dextran filled the
325 enlarged flagellar pocket while ConA was restricted to one or two small foci that appeared to
326 be on the cell surface (Fig. 7B, +Tet, arrow). No overlap was seen between the dextran and
327 ConA labels, suggesting that ConA was not able to enter the flagellar pocket. In addition, no
328 overlap was observed between ConA and the lysosome marker p67 (Fig. S8, +Tet cells).
329
330 To quantify these observations, the cells were grouped into 4 categories: 1, complete overlap
331 between the two labels; 2, partial overlap between the two labels; 3, no overlap between the
332 two labels; 4, whole-cell labelling. Control (-Tet) cells all showed complete overlap between

333 the dextran and ConA, while cells depleted of TbSmee1 for 24 h showed >25% of cells with
334 partial or no overlap between the cargoes (Fig. 7C).
335
336 To further validate these observations, the experiments were repeated using fluorescently-
337 labelled BSA (Fig. 7D). BSA traffics in the fluid phase and is a physiological cargo, unlike
338 ConA (Coppens et al., 1987). As expected, in control cells there was strong overlap between
339 dextran and BSA from the endosomal/lysosomal system (Fig. 7E, -Tet, arrow). In TbSmee1-
340 depleted cells, there was once again no overlap between the reporters, indicating that BSA
341 was unable to access the enlarged flagellar pocket. Surprisingly, despite BSA being fluid-
342 phase cargo there was a punctate signal analogous to that seen with ConA, suggesting that
343 it could at least partly bind to the cell surface (Fig. 7E, +Tet, arrow). Quantification of the data
344 showed that the effect on BSA was more pronounced than that seen for ConA, with >55% of
345 TbSmee1-depleted cells showing no or only partial overlap between the two reporters after 24
346 h of RNAi (Fig. 7F).
347
348
349 **Endocytosis is required for flagellar pocket access of surface-bound cargo.**
350 The inability of surface-bound cargo to enter the flagellar pocket of TbMORN1- and TbSmee1-
351 depleted cells could either be due to a defect in endocytosis (indicated by the enlargement of
352 the flagellar pocket), or a secondary effect.
353
354 To distinguish between these possibilities, the assays were repeated following clathrin
355 depletion (Fig. 8). Clathrin is an essential endocytic coat protein and its loss results in a block
356 in endocytosis. As expected, in control cells there was strong overlap between the dextran
357 and ConA cargoes (Fig. 8B, -Tet, arrow). In clathrin-depleted cells however, there was again
358 no overlap observed between the two reporters and ConA did not appear able to access the
359 enlarged flagellar pocket (Fig. 8B, +Tet, arrow). Quantification of the data showed that >50%
360 of clathrin-depleted cells showed either partial or no overlap between the two reporters after
361 19 h of RNAi (Fig. 8C). The same effect was seen in assays using dextran and BSA, with little
362 to no overlap between the reporters in clathrin-depleted cells (Fig. 8D-F). These results
363 indicated that inhibition of endocytosis by itself resulted in the failure of either ConA or BSA to
364 enter the enlarged flagellar pocket.
365
366
367 **Discussion**
368 In this study, the hook complex component TbSmee1 was characterised in bloodstream form
369 *T. brucei*. It is only the second hook complex protein to be characterised in this life cycle stage

370 after TbMORN1, and like TbMORN1 it is essential for the viability of the cells in vitro. The
371 localisation of TbSmee1 was found to be identical to that previously documented in the
372 procyclic life cycle stage of *T. brucei* (Figs 2, 3). It is constitutively present at the shank part of
373 the hook complex and probably also the FAZ tip, and additionally localises to the tip of the
374 growing new FAZ in replicating cells.
375
376 The analysis of truncation constructs suggested that different parts of the TbSmee1 primary
377 structure are responsible for targeting to the two locations (Figs 4, S5). Targeting to the hook
378 complex is mediated by the second and third predicted domains of TbSmee1. It is currently
379 not clear whether the linker region between these two domains (aa 401-630) is also required,
380 and this would be an obvious hypothesis to test in future work. Targeting to the FAZ tip appears
381 to be mediated by the linker region (aa 161-265) between the first and second predicted
382 domains. This is somewhat surprising, as there are few highly-conserved residues in this
383 region (Fig. S1). It should be noted that while aa 161-265 have been shown to be necessary
384 for FAZ tip targeting, they have not yet been shown to be sufficient - this again would be an
385 obvious future experiment should this line of enquiry be pursued further.
386
387 Phenotypic characterisation of TbSmee1 showed that its depletion results in the enlargement
388 of the flagellar pocket with concomitant effects on the entry of macromolecular cargo (Figs 5-
389 7). A clear limitation of all the RNAi experiments was the inability to specifically isolate cells
390 with reduced levels of TbSmee1. As the cells were being assayed very soon after the onset
391 of the growth defect, this meant that all assays were being conducted against a background
392 of cells exhibiting different and often much lower levels of TbSmee1 depletion. This could be
393 addressed in future experiments either by using a fluorescent tag on TbSmee1 to enable
394 sorting of the subpopulation of depleted cells, or by synchronising the cells prior to the
395 induction of RNAi. Nonetheless, there was still extremely good correlation between the
396 immunoblotting, growth curve, and cell cycle analysis data in these experiments.
397
398 At 18 h post-induction of RNAi, TbSmee1 protein levels were reaching their minimum but there
399 was as yet no observable effect on cell cycle progression or population growth. From around
400 20/21 h post-induction, when TbSmee1 levels reached 10-15% of controls, cell cycle
401 progression slowed, resulting in an increase in 2K1N and 2K2N cells. This was mirrored by a
402 slowing of population growth. Systematic analysis of a number of marker proteins for the hook
403 complex, the centrin arm, and the flagellar pocket collar showed that none were strongly
404 affected in terms of their protein levels or localisation by the depletion of TbSmee1. This
405 argues that the effects seen upon TbSmee1 depletion at these early timepoints are probably
406 due to a loss of function, rather than due to structural perturbations.

407
408 Flow cytometry analysis indicated that the flagellar pocket enlargement began around 18 h
409 post-induction, just prior to the effects on population growth and cell cycle progression. This
410 therefore suggests that flagellar pocket enlargement is an early and likely direct consequence
411 of TbSmee1 depletion. One plausible hypothesis to account for these observations is that the
412 geometric problems entailed by flagellar pocket enlargement may lead to the subsequent
413 delay in cell cycle progression and population growth.
414
415 The enlargement of the flagellar pocket was accompanied by a cargo access defect previously
416 documented for TbMORN1 - small fluid-phase cargo such as 10 kDa dextran fills the enlarged
417 flagellar pocket, while larger cargo such a ConA and BSA is unable to (Morriswood and
418 Schmidt, 2015). In TbSmee1-depleted cells, BSA was observed in one or more small foci next
419 to the flagellar pocket. This was surprising, as BSA is known to traffic in the fluid phase and
420 should not therefore be binding to the cell surface. BSA was however also observed to
421 associate with the flagellar pocket membrane in an electron microscopy-based study of cargo
422 uptake (Gadelha et al., 2009). In a classic radiochemical study of cargo uptake in *T. brucei,* it
423 was observed that "at low concentration, a small adsorbtive component may become
424 prevailing" in assays using BSA (Coppens et al., 1987). As the experiments conducted here
425 and in the 2009 paper were using BSA well below physiological concentrations, it seems likely
426 that these foci represent the small adsorbtive component that was indirectly observed in the
427 biochemical assays. Therefore, in these assays, the ConA and BSA probes both report on the
428 behaviour of surface-bound cargo, while the dextran reports on fluid-phase uptake.
429
430 Analysis of clathrin-depleted cells indicated that impairment of endocytosis is most likely
431 responsible for the defect in entry of surface-bound cargo. These data contradict previously-
432 published observations, where ConA was claimed to accumulate inside the enlarged flagellar
433 pocket of clathrin-depleted cells (Allen et al., 2003). Re-examination of previously-published
434 data from clathrin RNAi cells suggests however that the effect has always been present, with
435 ConA signal (and indeed other cargoes) absent from the flagellar pocket interior and
436 predominantly concentrated in one or more foci just outside it (see for example Fig. S4 in
437 (Allen et al., 2003), and Fig. S2 in (Zoltner et al., 2015)). This oversight is understandable,
438 given that the focus in these clathrin papers was on whether or not cargo endocytosis was
439 occurring, and not whether the cargo was able to access the flagellar pocket (Mark Field,
440 personal communication). Importantly, it also means that similar observations have been
441 made by (at least) two independent groups.
442

443 It has been known for some time that surface-bound cargo in the lumen of the flagellar pocket
444 is associated with the membrane underlying the microtubule quartet (Brickman and Balber,
445 1990; Gadelha et al., 2009). It has also previously been shown that upon inhibition of
446 endocytosis, tomato lectin, wheat germ agglutinin, and BSA accumulate on this part of the
447 flagellar pocket membrane (Gadelha et al., 2009). What is intriguing about the observations
448 with TbSmee1 and clathrin RNAi cells here is that they show that fluid phase cargo (dextran)
449 is still able to enter the flagellar pocket even when endocytosis is inhibited, so the effects are
450 specific to surface-bound cargo. Given that the ConA and BSA material becomes
451 concentrated into one or more foci that do not overlap with the dextran signal (Figs 7,8), this
452 suggests that the majority of cargo is not able to enter the flagellar pocket lumen at all when
453 endocytosis is inhibited.
454
455 This begs two important questions: why is it that an inhibition of endocytosis apparently
456 hinders the entry of surface-bound cargo into the flagellar pocket? And why does the depletion
457 of hook complex proteins - which are spatially removed from the actual sites of clathrin-coated
458 vesicle formation - cause an endocytosis defect? The prevailing model for several years has
459 been that hydrodynamic flow, driven by flagellar motility, is responsible for sorting surface-
460 bound cargo to the posterior end of the cell where the flagellar pocket is located (Engstler et
461 al., 2007). Once there, the surface-bound material enters the flagellar pocket through a narrow
462 channel where the flagellar membrane and the flagellar pocket neck membrane are not as
463 closely apposed (Gadelha et al., 2009).The results here suggest that the posterior sorting
464 mechanism still functions when endocytosis is inhibited, but that the transit of surface-bound
465 material through the channel is impeded. The fact that fluid phase cargo still enters the
466 enlarging flagellar pockets demonstrates that the channel lumen must still be open.
467
468 An earlier hypothesis for hook complex function was that it was somehow maintaining the
469 integrity of the channel in the flagellar pocket neck. This remains possible - and determining
470 the exact site of cargo blockade, as well as imaging the microtubule quartet, will be key goals
471 for future work - but the fact that the same phenotype is obtained following depletion of clathrin
472 suggests that the hook complex is instead indirectly affecting endocytosis. This could
473 potentially be by affecting either the localisation or activity of a number of lipid kinases, at least
474 two of which are known to localise to the hook complex (Dean et al., 2017; Demmel et al.,
475 2014). It appears therefore that while hydrodynamic flow may be responsible for concentrating
476 cargo at the entrance to the flagellar pocket, endocytic activity is required for the entry of the
477 cargo into the flagellar pocket itself, and that endocytosis may assist or be responsible for
478 pulling material in through the channel. Exploring these mechanisms is likely to be a
479 fascinating area for future enquiry.

480
481
482 **Materials and Methods**
483
484 **Recombinant protein expression and purification**
485 The TbSmee1(1-400) open reading frame was amplified from *Trypanosoma brucei brucei*
486 strain Lister 427 genomic DNA by PCR. The PCR product was ligated into the p3NH
487 expression vector, which encodes an N-terminal His6 tag, using sequence and ligation-
488 independent cloning (Li and Elledge, 2012). The plasmid was used to transform *E. coli* strain
489 Rosetta II (DE3)pLysS by heat shock, and individual colonies were subsequently grown at 37
490 °C in the presence of 100 µg/ml kanamycin to an OD600 ~ 0.8–1.0. Recombinant protein
491 expression was induced by the addition of 50 µM IPTG, and the cells were then incubated
492 overnight at 20 °C with shaking. Cells were harvested by centrifugation (5000× g for 30 min).
493 The pooled pellet from 6 L of cell culture was resuspended in 300 ml of lysis buffer (50 mM
494 Hepes pH 7.0, 500 mM NaCl, 20 mM imidazole, 5% glycerol, 0.5% Triton-X, 1 mM TCEP, 200
495 mM PMSF and protease inhibitor cocktail). Pellet emulsions were first homogenised by mixing
496 on ice using a T 10 basic Ultra-Turrax dispersing instrument (IKA). Final lysis was then
497 achieved with sonication on ice, using 3 cycles of 3 min at 50% strength. Lysates were clarified
498 by centrifugation (18,000× g, 45 min, 4 °C). The lysates were added to a HiTrap Chelating HP
499 5 ml column (GE Healthcare) equilibrated with buffer A (20 mM Hepes pH 7, 300 mM NaCl,
500 40 mM imidazole, 2% glycerol, 1 mM TCEP), and eluted with a 100% step gradient of buffer
501 B1 (20 mM Hepes pH 7, 300 mM NaCl, 400 mM imidazole, 2% glycerol, 1 mM TCEP).
502 Selected peak fractions were examined by SDS-PAGE for protein content and purity.
503 Fractions containing a dominant band at approximately 46 kDa were pooled and concentrated
504 using Amicon Ultra centrifugal filter units with 10K pore size (MerckMillipore) according to the
505 manufacturer's instructions. The His6 tag was removed by 3C protease during overnight
506 dialysis in dialysis buffer (20 mM Tris-HCl pH 7, 300 mM NaCl, 2% glycerol, 1 mM DTT).
507 Significant losses were incurred during this step. The TbSmee1(1-400) was applied to a
508 previously equilibrated HiTrap Chelating HP 5 ml column charged with 50 mM $CoCl_2$ and
509 coupled to a GSTrap HP 1 ml column (both GE Healthcare). Buffer A was used for
510 equilibration. TbSmee1(1-1400) was mostly collected from the flow-through and a few initial
511 collected fractions. Selected peak fractions were examined by 15% SDS-PAGE for protein
512 content and purity. Fractions containing a dominant band at approximately 44 kDa were
513 pooled and concentrated in Amicon Ultra centrifugal filter units (10K pore size) according to
514 the manufacturer's instructions. Finally, TbSmee1(1-400) concentrates were applied to a
515 previously equilibrated HiLoad 16/600 Superdex 200 pg column (GE Healthcare) pre-
516 equilibrated in dialysis buffer. Flow speed was adjusted to 1 ml/min and fractions of 1.5 ml

517 were collected. Fractions corresponding to the targeted chromatographic peak were examined
518 for protein content by 15% SDS-PAGE, pooled accordingly to their purity, concentrated, and
519 stored at -80 °C.
520
521 **Antibody generation and affinity purification**
522 Purified recombinant TbSmee1(1-400) was used for the generation of two polyclonal rabbit
523 antisera (Eurogentec). Antisera were initially affinity-purified against the TbSmee1(1-400)
524 antigen, but the neat antisera were later found to show high specificity and were also used. A
525 third polyclonal antibody was generated against two TbSmee1 peptides (Eurogentec) and
526 affinity purified using the peptide antigens immonilised on a Sulfolink affinity column
527 (ThermoFisher). The anti-Starkey1 rabbit polyclonal antibodies were generated and affinity
528 purified in the same way.
529
530 **Antibodies**
531 The following primary antibodies have been described previously: rabbit anti-TbMORN1
532 (Morriswood et al., 2013), rabbit anti-TbBILBO1 (Esson et al., 2012), mouse anti-Ty1 ("BB2")
533 (Bastin et al., 1996), mouse anti-TbLRRP1 (Zhou et al., 2010), mouse anti-TbCentrin4 ("6C5"
534 (Ikeda and de Graffenried, 2012)), mouse anti-TbCentrin2 ("2B2H1") (de Graffenried et al.,
535 2013), mouse anti-TbFAZ1 ("L3B2") (Kohl et al., 1999), mouse anti-PFR1,2 ("L13D6") (Kohl
536 et al., 1999), mouse anti-FAZ filament ("DOT1")(Woods et al., 1989). The following antibodies
537 came from commercial sources: goat anti-rabbit(IRDye800CW) (LI-COR), goat anti-mouse
538 (IRDye680LT) (LI-COR), goat anti-rabbit and anti-mouse antibodies conjugated to AlexaFluor
539 dyes (Molecular Probes).
540
541 **Cell culture**
542 Wildtype 427 (monomorphic) BSF cells were cultured in HMI-9 medium (Hirumi and Hirumi,
543 1989) supplemented with 10 % foetal bovine serum (FBS), 100 U/ml penicillin and 0.1 mg/ml
544 streptomycin at 37°C and 5% CO_2. The SM (single marker) cells (Wirtz et al., 1999) were
545 cultured in the presence of G418 (2.5 µg/ml). Population density was monitored using a Z2
546 Coulter Counter (Beckman Coulter), and kept below $2x10^6$ cells/ml.
547
548 **Generation of transgenic cell lines**
549 The Ty1-TbSmee1 endogenous replacement cell line was generated by transfection of 427
550 cells with a targeting fragment containing 285 bp of the TbSmee1 5' untranslated region
551 (UTR), a blasticidine resistance gene, the intergenic region of alpha- and beta-tubulin, the
552 sequence for a triple Ty1-tag and the first 399 bp of the TbSmee1 open reading frame (ORF)
553 without the start codon. Clones were selected by growth in medium containing 5 µg/ml

554 blasticidine. RNAi target sequences were chosen using RNAit (Redmond et al., 2003).
555 TbSmee1 RNAi cells were generated by cloning the RNAi target sequence into the pGL2084
556 plasmid (Jones et al., 2014) and then transfecting 2T1 cells with the linearised plasmid (Alsford
557 et al., 2005). Clones were selected by growth in medium containing phleomycin (2.5 µg/ml)
558 and hygromycin (5 µg/ml). TbStarkey1 RNAi cells and TbCHC RNAi cells were generated by
559 cloning the relevant RNAi target sequence into the p2T7_TAblue plasmid (Alibu et al., 2005)
560 and then transfecting SM cells with the linearised plasmid. Clones were selected by growth in
561 medium containing G418 (2.5 µg/ml) and hygromycin (5 µg/ml). Ty1-TbSmee1 truncation
562 constructs were cloned into the pLew100_v5-Hyg plasmid using in vivo assembly (Watson
563 and Garcia-Nafria, 2019). SM cells were transfected with the linearised plasmid. Clones were
564 selected by growth in medium containing G418 (2.5 µg/ml) and hygromycin (5 µg/ml). For
565 transfection >2.5 × 10^7 cells of the parental strain were washed and resuspended in 100 µl
566 transfection buffer (90 mM Na_2PO_4, 5 mM KCl, 0.15 mM $CaCl_2$, 50 mM HEPES [4-(2-
567 hydroxyethyl)-1-piperazineethanesulfonic acid]-NaOH, pH 7.3) containing 10 µg DNA and
568 transfected by electroporation using an AMAXA Nucleofector® Device (Lonza) with program
569 "X-001 free choice". Transfected cells were incubated in 50 ml HMI-9 medium without
570 selection overnight. The next day, drug selection was applied and clones were selected by
571 limiting dilution. At least three separate clones of all cell lines were isolated to control for
572 biological variability. Integration of targeting fragments at endogenous loci or the presence of
573 Ty1-TbSmee1 truncation constructs in the genome were confirmed by PCR analysis of
574 genomic DNA. Genomic DNA was isolated using a DNeasy Bloody & Tissue kit (QIAGEN)
575 and relevant products were amplified by PCR. All cloned constructs used for cell line
576 generation had their DNA sequence confirmed by sequencing.

577 **Immunoblotting**

578 For generation of dephosphorylated whole-cell lysates, cells were harvested by centrifugation
579 (1000xg, 10 min) and the cell pellet was resuspended in 1 ml vPBS (PBS, 46 mM sucrose, 10
580 mM glucose) containing EDTA-free protease inhibitors (Roche). The washed cells were
581 pelleted by centrifugation (750xg, 4 min). The cells were then resuspended in lysis buffer
582 (0.5% IGEPAL, 0.1M PIPES-NaOH pH 6.9, 2 mM EGTA, 1 mM MgCl2, 0.1 mM EDTA, EDTA-
583 free protease inhibitor cocktail) to a final concentration of 4x10^5 cells/µl and incubated for 15
584 min at RT on an orbital mixer to allow dephosphorylation to occur. SDS-loading buffer was
585 then added to a final concentration of 2x10^5 cells/µl, the samples were further denatured by
586 boiling (100°C, 10 min), and then stored at -20°C. SDS-PAGE was carried out using a Mini-
587 Protean Tetra Cell (Bio-Rad), and protein transfer to nitrocellulose membranes using a Mini-
588 Trans blot cell (Bio-Rad). Protein transfer and equal loading was confirmed using REVERT

589 total protein stain (LI-COR) according to the manufacturer's instructions. Membranes were
590 blocked using blocking buffer (PBS, 0.3% Tween 20, 10% milk)(30 min, RT, rocker). The
591 membranes were then incubated in primary antibodies diluted in blocking buffer (1 h, RT,
592 roller). After three washes in immunoblot buffer (PBS, 0.3% Tween 20) the membranes were
593 incubated with IRDye-conjugated secondary antibodies diluted in immunoblot buffer (1 h, RT,
594 roller). After another three washes in immunoblot buffer, the membranes were visualised using
595 an Odyssey CLx (LI-COR). Background subtraction, qualitative analysis, normalisation
596 relative to total protein stain, and quantification were carried out using Image Studio Lite 5.2
597 and Empiria Studio 1.1 (LI-COR). Dot plots were generated using the web app PlotsOfData
598 (Postma and Goedhart, 2019).

599 **In vitro phosphatase assays**

600 427 BSF cells were grown to approximately $1.5x10^6$ cells/ml and harvested by centrifugation
601 (1,000xg, 10 min, 4 °C). The cells were washed in 1 ml ice-cold wash buffer (0.1M PIPES-
602 NaOH pH 6.9, 2 mM EGTA, 1 mM MgCl2, 0.1 mM EDTA, phosphatase Inhibitor Cocktail 2)
603 and pelleted by centrifugation (750xg, 3 min, 4 °C). For extraction of the cytoskeletons, the
604 cell pellet was resuspended in 1ml ice-cold extraction buffer (0.5% IGEPAL, 0.1M PIPES-
605 NaOH pH 6.9, 2 mM EGTA, 1 mM MgCl2, 0.1 mM EDTA, EDTA-free protease inhibitor
606 cocktail, phosphatase Inhibitor Cocktail 2) and incubated for 15 min on ice. The cell
607 suspension was inverted every 5 min. The cytoskeletons were separated from the cytoplasm
608 by centrifugation (750xg, 3 min, 4 °C). The cytoskeletons were washed with 0.5 ml ice-cold 1x
609 NEBuffer for PMP supplemented with 1 mM $MnCl_2$ and pelleted by centrifugation (750xg, 3
610 min, 4 °C). After resuspension in 375 µl ice-cold 1x NEBuffer for PMP supplemented with 1
611 mM $MnCl_2$, all following samples were taken from this stock. An input sample (0 min) of 40 µl
612 was taken and added to 20 µl of SDS-loading buffer. Two control samples were taken, 0.4 µl
613 Phosphatase Inhibitor Cocktail 2 was added, and incubated on ice and at 26°C, respectively,
614 for 20 min. 20 µl of SDS-loading buffer was then added. To assay for dephosphorylation, 130
615 µl were taken from the stock and 1 µl lambda phosphatase (400 U) was added. This sample
616 and the remainder from the stock were incubated at 26 °C. After 1/2/3/5/10/20 min 20 µl
617 samples were taken from each and were added to 10 µl SDS-loading buffer. All the samples
618 were boiled at 104 °C for 10 min and stored at -20 °C. Samples were analysed by
619 immunoblotting.

620 **Fractionation**

621 50 ml 427 BSF cells were grown to approximately $1.5x10^6$ cells/ml and then harvested by
622 centrifugation (1000xg, 10 minutes, 4°C). The cell pellet was resuspended in 1 ml vPBS,

623 transferred to a microfuge tube, and the cells again pelleted by centrifugation (750xg, 4 min,
624 4°C). The supernatant was discarded and the centrifugation step was repeated to remove
625 remaining supernatant. The cell pellet was resuspended in 200 µl extraction buffer (0.5%
626 IGEPAL, 0.1M PIPES-NaOH pH 6.9, 2 mM EGTA, 1 mM MgCl2, 0.1 mM EDTA, EDTA-free
627 protease inhibitor cocktail) and incubated for 15 minutes at RT in an orbital mixer. A 5% input
628 sample was taken (10µl), put into a new microfuge tube and left on ice. The extracted cells
629 were fractionated by centrifugation (3400xg, 2 minutes, 4°C) and the supernatant transferred
630 to a fresh microfuge tube and the exact volume noted. The tube containing the extracted cells
631 was centrifuged again at the same settings and this second residual supernatant discarded.
632 The cytoskeleton pellet was then resuspended in 200 µl extraction buffer. 5% samples of
633 supernatant and pellet fractions were taken and analysed by immunoblotting. Equal fractions
634 of I, SN, P were loaded in each lane (I ~ $1.4x10^6$ cells).

635 **Preparation of samples for immunofluorescence microscopy**

636 Coverslips were washed in 70% ethanol and then incubated with 0.01% poly-L-lysine in a 24-
637 well plate (>20 min, RT) and left to dry. $2x10^6$ cells were taken per coverslip and transferred
638 to 15 ml Falcon tubes. The cells were pelleted by centrifugation (1000xg, 1 min per ml of liquid,
639 RT) in a swing-bucket centrifuge. The supernatant was removed, and the cell pellet was gently
640 resuspended in 1 ml ice-cold vPBS + Complete. The cells were again pelleted by
641 centrifugation (1000xg, 2 min, RT) and subsequently resuspended in 1 ml ice-cold vPBS +
642 Complete and directly added to the coverslips. The cells were attached to the coverslips by
643 centrifugation (1000xg, 1 min, RT), and attachment was confirmed visually. The attached cells
644 were then incubated in 1 ml ice-cold extraction buffer (0.5% IGEPAL 0.1M PIPES-NaOH pH
645 6.9, 2 mM EGTA, 1 mM MgCl2, 0.1 mM EDTA, EDTA-free protease inhibitor cocktail) (5 min,
646 on ice). The extracted cells were washed two times with 1 ml vPBS + Complete and then fixed
647 in 1 ml ice-cold 99.9% methanol (30 min, -20°C). The fixed cells were rehydrated using 1 ml
648 PBS. The coverslips were blocked in 1 ml 3% BSA in PBS (30 min, RT), and sequentially
649 incubated with clarified primary and secondary antibodies diluted in PBS (1 h, RT, humidified
650 chamber for each) with three PBS washing steps (3 x 5 min, RT, rocker) after each incubation.
651 After the final wash, glass slides were cleaned with 70% ethanol and a spot of DAPI-
652 Fluoromount G (Southern Biotech) was placed on the surface. The coverslips were rinsed in
653 ddH_2O, carefully dried, and then mounted. For preparation of samples for SIM imaging,
654 different coverslips (high precision, No. 1.5 H) were used. Cells were harvested as above,
655 washed, and fixed in 4% paraformaldehyde solution (10 min, ice then 30 min, RT). The fixed
656 cells were washed, attached to coverslips, permeabilised (0.25% Triton X-100 in PBS; 5 min,
657 RT), and then labelled and mounted as described above.

658 **Fluorescence microscopy**

659 Images were acquired using a DMI6000B widefield microscope (Leica Microsystems,
660 Germany) with a HCX PL APO CS objective (100x, NA = 1.4, Leica Microsystems, Germany)
661 and Type F Immersion Oil (refractive index = 1.518, Leica Microsystems, Germany). The
662 microscope was controlled using LAS-X software (Leica). Samples were illuminated with an
663 EL6000 light source (Leica) containing a mercury short-arc reflector lamp (HXP-R120W/45C
664 VIS, OSRAM, Germany). Excitation light was selected by using Y3 (545/25 nm), GFP (470/40
665 nm), and A4 (360/40 nm) bandpass filter cubes (Leica Microsystems, Germany). The power
666 density, measured at the objective focal plane with a thermal sensor head (S175C, Thorlabs),
667 was respectively 0.749 ± 0.086, 0.557 ± 0.069, 0.278 ± 0.076 W/cm^2 for the three filters.
668 Emitted light was collected at ranges of 605/70 (Y3), 525/50 nm (GFP), and 470/40 nm (DAPI)
669 respectively. The individual exposure times and camera gains were adjusted according to the
670 different samples. RNAi samples (control and depleted) were imaged using identical settings.
671 Differential interference contrast (DIC) was used to visualise cell morphology. 3D recording of
672 each field of view was obtained using 40 Z-slices (step size = 0.21 µm). Fields of view were
673 selected in the DIC channel in order to blind the user to the fluorescence signal and
674 subjectively select for cells with optimum morphology. Images were captured using a DFC365
675 FX monochrome CCD camera (Leica, 6.45 µm pixel size). SIM images were acquired using
676 an Elyra S.1 SIM microscope (Zeiss) and ZEN software (Zeiss).

677

678 **Fluorescence microscopy image processing and analysis**

679 Processing was carried out using FIJI (Schindelin et al., 2012) and a custom macro for the
680 generation of maximum-intensity z-projections with single DIC z-slices overlaid. Overlaps
681 between two proteins were confirmed in individual z-slices (thickness: 210 nm). The plugin
682 ScientiFig was utilised to create the collage and adding the inserts (Aigouy and Mirouse,
683 2013). For global correlation analysis between TbSmee1 and other flagellar pocket collar
684 and/or hook complex associated proteins, 1K1N cells were selected using both DIC and DAPI
685 channels. 2D sum slices projections were prepared for each stack of both green and red
686 channels. The projections were clipped to 8-bit depth and a convoluted background
687 subtraction was applied. All resultant 2D images were analysed individually, without channel
688 overlay, and each selected cell had the intensity values of both channels acquired from the
689 histogram. In order to check for data distribution and to determine the suitable correlation
690 method (Aaron et al., 2018; Dunn et al., 2011), the intensity values were further analyzed in R
691 version 4.1.2 (Team, 2021) using the packages ggplot2 (H, 2016) and openxlsx (Schauberger,
692 2021). The normality was checked by visual inspection of q-q plots and the correlation was
693 tested using Spearman's rank correlation. A scatter plot using the intensity values (green x
694 red) was generated to each protein against Smee1. To visualise the variation of the correlation

695 within the sample population, a scatter plot of the correlation coefficient obtained per individual
696 cell was prepared.
697
698 **Growth curves**
699 RNAi cells were seeded at the required starting concentration in a volume of 22 ml and divided
700 into two 10 ml aliquots in separate flasks. Tetracycline was added to a final concentration of 1
701 µg/ml in one flask to induce RNAi, and refreshed every 24h. The population density of the
702 control and induced cells was measured every 24h over a time course of 72h, or every hour
703 over a time course of 8h, using a Z2 Coulter Counter (Beckman Coulter). Depletion of the
704 target protein was confirmed in every experiment by immunoblotting of whole-cell lysates.
705
706 **Cell division cycle analysis**
707 An aliquot of 10^6 cells was taken, and the cells were fixed directly in media by addition of
708 isothermal 25% glutaraldehyde to a final concentration of 2.5% (10 min, 37°C, gentle mixing).
709 The cells were then pelleted by centrifugation (750xg, 10 min). The cell pellet was
710 resuspended in 0.5 ml 2.5% glutaraldehyde in PBS, transferred to a microfuge tube, and
711 incubated at RT (30 min, gentle mixing). The cells were pelleted again by centrifugation
712 (750xg, 4 min), and the cell pellet resuspended in 500 µl PBS. The cells were then added to
713 the coverslips inside the 24-well plate and attached by centrifugation (1000xg, 1 min, RT). The
714 coverslips were mounted on poly-L-lysine-coated slides using DAPI-Fluoromount G (Southern
715 Biotech). Imaging was as described for fluorescence microscopy above, using DAPI and DIC
716 channels only. Cell division cycle stages (1K1N, 2K1N, 2K2N) were manually quantified from
717 maximum intensity projections of the DAPI signal overlaid with single DIC z-slices. Depletion
718 of the target protein at each timepoint was confirmed by immunoblotting of whole-cell lysates
719 from the same experiments.
720
721 **Preparation and imaging of electron microscopy samples**
722 Induced and uninduced RNAi cells were grown for 24 h to a density of 1-2x10^6 cells/ml in 50
723 ml medium and harvested by centrifugation (1000xg, 10 min, RT). The supernatant was
724 removed to 4 ml and 4 ml FBS was added. The cells were pelleted again (1000xg, 10 min,
725 RT) and the supernatant was removed to 200 µl. The cells were resuspended in the
726 supernatant, and the suspension was then transferred to a PCR tube and pelleted by
727 centrifugation (1,600xg, 10s, RT). The cells were then transferred into a carrier with a closed
728 lid to avoid air inclusions. High pressure freezing (HPF) was started immediately (Leica EM
729 HPM100). After HPF the samples were transferred to an AFS (Leica EM AFS2) for freeze
730 substitution and progressive lowering of temperature. Low temperature embedding and
731 polymerisation of Epon raisin (DDSA, MNA, Epon812, 2,4,6

732 Tris(dimethylaminomethyl(phenol))) were then carried out. Ultra-thin cuts (60 nm) were carried
733 out with an ultramicrotome (Leica EM UC7/FC7) and were placed on slotted grids. For
734 contrasting they were incubated in 2 % uranyl acetate for 8 min. Afterwards the grids were
735 washed 3x in ddH_2O (boiled to remove CO_2) and incubated for 5 min on 50 % Reynold's lead
736 citrate in a petri dish with NaOH tablets. The grids were again washed 2x in ddH_2O. A 200 kV
737 transmission electron microscope (Jeol, JEM-2100) with a TemCam F416 4k x 4k camera
738 (Tietz Video and Imaging Processing Systems) and EMMenu 4.0.9.31 software (Tietz) were
739 used. Uninduced control cells were viewed at a magnification of 12,000x, induced cells were
740 viewed at a magnification of 8,000x.
741
742 **Measurement of flagellar pocket enlargement**
743 Induced and uninduced RNAi cells at a concentration of ~5×10^6 cells/ml were harvested by
744 centrifugation (1000xg, 4 ºC). The cells were resuspended in 45 µl ice-cold vPBS + protease
745 inhibitors and incubated on ice to block endocytosis (10 min, ice). 5 µl labelled dextran (10
746 kDa, 50 mg/ml stock) was added and mixed by flicking. The mixture was then incubated to
747 allow dextran to enter and fill the flagellar pocket (15 min, on ice, dark). At the end of the
748 incubation, 1 ml ice-cold vPBS + protease inhibitors was added and the cells pelleted by
749 centrifugation (750 x*g*, 2 min, 4 ºC). The cell pellet was resuspended in 0.5 ml vPBS + protease
750 inhibitors, and the cells fixed by addition of 0.5 ml 8 % pfa and 0.1 % glutaraldehyde solution
751 in vPBS + protease inhibitors (20 min, on ice then 60 min, RT). The fixed cells were pelleted
752 by centrifugation (750 x*g*, 2 min) and washed twice with 1 ml vPBS + protease inhibitors. The
753 dextran signal was immediately measured by flow cytometry using a FACSCalibur (BD
754 Biosciences) running CellQuest ProTM Software (BD Biosciences). Later processing and
755 analysis was carried out using FlowJo 10.8.1. Dot plots were created using Plots of Data
756 (CITATION). After flow cytometry, the remaining cells were attached to coverslips by
757 centrifugation, mounted on clean glass slides using DAPI-Fluoromount G (Southern biotech),
758 and imaged using fluorescence microscopy on the same day to confirm flagellar pocket
759 labelling. Depletion of TbSmee1 was confirmed in every experiment by immunoblotting of
760 whole-cell lysates.
761
762 **Cargo uptake assays**
763 $2x10^6$ cells per sample were harvested by centrifugation (1000 xg, 10 min, 4 ºC) and washed
764 in 1 ml ice-cold vPBS. The washed cells were pelleted by centrifugation (750 xg, 2 min, 4 ºC),
765 and resuspended in 100 µl ice-cold vPBS. The cells were then incubated at low temperature
766 (20 min, ice) to block endocytosis. During this incubation, the labelled cargoes were prepared.
767 The 50 mg/ml dextran aliquot (10 kDa AF488 conjugate, Molecular Probes) was mixed using
768 a sonicator bath (10 min, 37 Hz) and then vortexed. The 0.5 mg/ml ConA aliquot (TMR

769 conjugate, Molecular Probes) was clarified by centrifugation (11,000 xg, 10 min, 4 ºC). Both
770 cargoes were kept on ice and in the dark. At the end of the incubation, 10 µl of the 50 mg/ml
771 dextran and 2 µl of the 0.5 mg/ml ConA were added to the chilled cells, mixed by flicking, and
772 incubated at low temperature (15 min, on ice, in the dark). T=0 samples were quenched and
773 fixed at this point; t=30 samples had an additional incubation to allow endocytosis of cargo (30
774 min, 37 ºC, in the dark) before quenching and fixing. To quench samples, 1 ml ice-cold vPBS
775 was added, and the cells were pelleted by centrifugation (750 xg, 2 min, 4 ºC). The pelleted
776 cells were resuspended in 50 µl vPBS by flicking, and then fixed by addition of 0.5 ml ice-cold
777 fix solution (4% paraformaldehyde solution, 0.1% glutaraldehyde in vPBS) (20 min, on ice, in
778 the dark, then 30 min, RT, in the dark). The fixed cells were pelleted by centrifugation (750 xg,
779 2 min, RT), washed in 2 ml vPBS, resuspended in 1 ml vPBS, and then attached to poly-L-
780 lysine-coated coverslips by centrifugation. Coverslips were mounted on glass slides using
781 DAPI-Fluoromount G (Southern Biotech) and imaged immediately. Assays using BSA
782 (AlexaFluor555 conjugate, Molecular Probes) were done in the same way. The 20 mg/ml BSA
783 aliquot was clarified by centrifugation (750 xg, 1 min, RT)), and 3 µl was added to the
784 cells/dextran mixture. Depletion of TbSmee1 was confirmed by immunoblotting of whole-cell
785 lysates in every experiment.
786
787 **Acknowledgements**
788 Antibodies were obtained from the following sources: Cynthia He (National University of
789 Singapore) provided the anti-Ty1 (BB2) and anti-TbLRRP1 antibodies; Chris de Graffenried
790 (Brown University) provided the anti-TbCentrin2 (2B2H1) and anti-TbCentrin4 (6C5)
791 antibodies, Keith Gull (University of Oxford) provided the anti-FAZ1 (L3B2), anti-PFR1,2
792 (L13D6) and DOT1 antibodies. Nadine Weisert provided assistance with cloning. Markus
793 Engstler provided support and advice. Balázs Szöőr (University of Edinburgh) provided input
794 on the phosphatase assays. Mark Field (University of Dundee) provided extremely helpful
795 advice and context on earlier clathrin RNAi work. Tim Krüger provided input and assistance
796 with imaging. Helena Jambor (TU Dresden) advised on data visualisation. Graham Warren
797 (Max Perutz Laboratories) hosted the preliminary experiments for this project. Susanne
798 Kramer and Manfred Alsheimer provided feedback on the manuscript.
799
800 **Competing interests**
801 There are no competing interests to be declared.
802
803 **Funding**
804 Funding in the initial phase was from the Austrian Science Fund (FWF) grant P27016. Later
805 funding was from the German Research Foundation (DFG) grant Mo 3188/2-1.

806
807
808 **References**
809

810 **Aaron, J. S., Taylor, A. B. and Chew, T. L.** (2018). Image co-localization - co-occurrence
811 versus correlation. *Journal of cell science* **131**.
812 **Aigouy, B. and Mirouse, V.** (2013). ScientiFig: a tool to build publication-ready scientific
813 figures. *Nat Methods* **10**, 1048.
814 **Ali, M., Leung, K. F. and Field, M. C.** (2014). The ancient small GTPase Rab21 functions in
815 intermediate endocytic steps in trypanosomes. *Eukaryotic cell* **13**, 304-19.
816 **Alibu, V. P., Storm, L., Haile, S., Clayton, C. and Horn, D.** (2005). A doubly inducible system
817 for RNA interference and rapid RNAi plasmid construction in Trypanosoma brucei. *Molecular*
818 *and biochemical parasitology* **139**, 75-82.
819 **Allen, C. L., Goulding, D. and Field, M. C.** (2003). Clathrin-mediated endocytosis is essential
820 in Trypanosoma brucei. *The EMBO journal* **22**, 4991-5002.
821 **Alsford, S., Kawahara, T., Glover, L. and Horn, D.** (2005). Tagging a T. brucei RRNA locus
822 improves stable transfection efficiency and circumvents inducible expression position effects.
823 *Molecular and biochemical parasitology* **144**, 142-8.
824 **Bastin, P., Bagherzadeh, Z., Matthews, K. R. and Gull, K.** (1996). A novel epitope tag
825 system to study protein targeting and organelle biogenesis in Trypanosoma brucei. *Molecular*
826 *and biochemical parasitology* **77**, 235-9.
827 **Benz, C. and Urbaniak, M. D.** (2019). Organising the cell cycle in the absence of
828 transcriptional control: Dynamic phosphorylation co-ordinates the Trypanosoma brucei cell
829 cycle post-transcriptionally. *PLoS Pathog* **15**, e1008129.
830 **Bonhivers, M., Nowacki, S., Landrein, N. and Robinson, D. R.** (2008). Biogenesis of the
831 trypanosome endo-exocytotic organelle is cytoskeleton mediated. *PLoS biology* **6**, e105.
832 **Borst, P. and Fairlamb, A. H.** (1998). Surface receptors and transporters of Trypanosoma
833 brucei. *Annu Rev Microbiol* **52**, 745-78.
834 **Brickman, M. J. and Balber, A. E.** (1990). Trypanosoma brucei rhodesiense bloodstream
835 forms: surface ricin-binding glycoproteins are localized exclusively in the flagellar pocket and
836 the flagellar adhesion zone. *The Journal of protozoology* **37**, 219-24.
837 **Brickman, M. J., Cook, J. M. and Balber, A. E.** (1995). Low temperature reversibly inhibits
838 transport from tubular endosomes to a perinuclear, acidic compartment in African
839 trypanosomes. *Journal of cell science* **108 (Pt 11)**, 3611-21.
840 **Coppens, I., Opperdoes, F. R., Courtoy, P. J. and Baudhuin, P.** (1987). Receptor-mediated
841 endocytosis in the bloodstream form of Trypanosoma brucei. *J Protozool* **34**, 465-73.

842 **de Graffenried, C. L., Anrather, D., Von Raussendorf, F. and Warren, G.** (2013). Polo-like
843 kinase phosphorylation of bilobe-resident TbCentrin2 facilitates flagellar inheritance in
844 Trypanosoma brucei. *Molecular biology of the cell* **24**, 1947-63.
845 **Dean, S., Sunter, J. D. and Wheeler, R. J.** (2017). TrypTag.org: A Trypanosome Genome-
846 wide Protein Localisation Resource. *Trends Parasitol* **33**, 80-82.
847 **Demmel, L., Schmidt, K., Lucast, L., Havlicek, K., Zankel, A., Koestler, T., Reithofer, V.,**
848 **de Camilli, P. and Warren, G.** (2014). The endocytic activity of the flagellar pocket in
849 Trypanosoma brucei is regulated by an adjacent phosphatidylinositol phosphate kinase.
850 *Journal of cell science* **127**, 2351-64.
851 **Dunn, K. W., Kamocka, M. M. and McDonald, J. H.** (2011). A practical guide to evaluating
852 colocalization in biological microscopy. *Am J Physiol Cell Physiol* **300**, C723-42.
853 **Engstler, M., Pfohl, T., Herminghaus, S., Boshart, M., Wiegertjes, G., Heddergott, N. and**
854 **Overath, P.** (2007). Hydrodynamic flow-mediated protein sorting on the cell surface of
855 trypanosomes. *Cell* **131**, 505-15.
856 **Engstler, M., Thilo, L., Weise, F., Grunfelder, C. G., Schwarz, H., Boshart, M. and**
857 **Overath, P.** (2004). Kinetics of endocytosis and recycling of the GPI-anchored variant surface
858 glycoprotein in Trypanosoma brucei. *Journal of cell science* **117**, 1105-15.
859 **Esson, H. J., Morriswood, B., Yavuz, S., Vidilaseris, K., Dong, G. and Warren, G.** (2012).
860 Morphology of the trypanosome bilobe, a novel cytoskeletal structure. *Eukaryotic cell* **11**, 761-
861 72.
862 **Florimond, C., Sahin, A., Vidilaseris, K., Dong, G., Landrein, N., Dacheux, D., Albisetti,**
863 **A., Byard, E. H., Bonhivers, M. and Robinson, D. R.** (2015). BILBO1 Is a Scaffold Protein
864 of the Flagellar Pocket Collar in the Pathogen Trypanosoma brucei. *PLoS pathogens* **11**,
865 e1004654.
866 **Gadelha, C., Rothery, S., Morphew, M., McIntosh, J. R., Severs, N. J. and Gull, K.** (2009).
867 Membrane domains and flagellar pocket boundaries are influenced by the cytoskeleton in
868 African trypanosomes. *Proceedings of the National Academy of Sciences of the United States*
869 *of America* **106**, 17425-30.
870 **Grunfelder, C. G., Engstler, M., Weise, F., Schwarz, H., Stierhof, Y. D., Morgan, G. W.,**
871 **Field, M. C. and Overath, P.** (2003). Endocytosis of a glycosylphosphatidylinositol-anchored
872 protein via clathrin-coated vesicles, sorting by default in endosomes, and exocytosis via
873 RAB11-positive carriers. *Molecular biology of the cell* **14**, 2029-40.
874 **H, W.** (2016). ggplot2: Elegant Graphics for Data Analysis: Springer-Verlag New York.
875 **Hall, B., Allen, C. L., Goulding, D. and Field, M. C.** (2004). Both of the Rab5 subfamily small
876 GTPases of Trypanosoma brucei are essential and required for endocytosis. *Molecular and*
877 *biochemical parasitology* **138**, 67-77.

878 **Hall, B. S., Smith, E., Langer, W., Jacobs, L. A., Goulding, D. and Field, M. C.** (2005).
879 Developmental variation in Rab11-dependent trafficking in Trypanosoma brucei. *Eukaryotic*
880 *cell* **4**, 971-80.
881 **Halliday, C., Billington, K., Wang, Z., Madden, R., Dean, S., Sunter, J. D. and Wheeler, R.**
882 **J.** (2019). Cellular landmarks of Trypanosoma brucei and Leishmania mexicana. *Molecular*
883 *and biochemical parasitology* **230**, 24-36.
884 **Halliday, C., de Castro-Neto, A., Alcantara, C. L., Cunha, E. S. N. L., Vaughan, S. and**
885 **Sunter, J. D.** (2021). Trypanosomatid Flagellar Pocket from Structure to Function. *Trends*
886 *Parasitol* **37**, 317-329.
887 **Hirumi, H. and Hirumi, K.** (1989). Continuous cultivation of Trypanosoma brucei blood stream
888 forms in a medium containing a low concentration of serum protein without feeder cell layers.
889 *J Parasitol* **75**, 985-9.
890 **Hughes, L., Towers, K., Starborg, T., Gull, K. and Vaughan, S.** (2013). A cell-body groove
891 housing the new flagellum tip suggests an adaptation of cellular morphogenesis for parasitism
892 in the bloodstream form of Trypanosoma brucei. *Journal of cell science* **126**, 5748-57.
893 **Ikeda, K. N. and de Graffenried, C. L.** (2012). Polo-like kinase is necessary for flagellum
894 inheritance in Trypanosoma brucei. *Journal of cell science* **125**, 3173-84.
895 **Jones, N. G., Thomas, E. B., Brown, E., Dickens, N. J., Hammarton, T. C. and Mottram,**
896 **J. C.** (2014). Regulators of Trypanosoma brucei cell cycle progression and differentiation
897 identified using a kinome-wide RNAi screen. *PLoS Pathog* **10**, e1003886.
898 **Kelley, R. J., Alexander, D. L., Cowan, C., Balber, A. E. and Bangs, J. D.** (1999). Molecular
899 cloning of p67, a lysosomal membrane glycoprotein from Trypanosoma brucei. *Molecular and*
900 *biochemical parasitology* **98**, 17-28.
901 **Kohl, L., Sherwin, T. and Gull, K.** (1999). Assembly of the paraflagellar rod and the flagellum
902 attachment zone complex during the Trypanosoma brucei cell cycle. *J Eukaryot Microbiol* **46**,
903 105-9.
904 **Lacomble, S., Vaughan, S., Gadelha, C., Morphew, M. K., Shaw, M. K., McIntosh, J. R.**
905 **and Gull, K.** (2009). Three-dimensional cellular architecture of the flagellar pocket and
906 associated cytoskeleton in trypanosomes revealed by electron microscope tomography.
907 *Journal of cell science* **122**, 1081-90.
908 **Li, M. Z. and Elledge, S. J.** (2012). SLIC: a method for sequence- and ligation-independent
909 cloning. *Methods Mol Biol* **852**, 51-9.
910 **Link, F., Borges, A. R., Jones, N. G. and Engstler, M.** (2021). To the Surface and Back:
911 Exo- and Endocytic Pathways in Trypanosoma brucei. *Front Cell Dev Biol* **9**, 720521.
912 **McAllaster, M. R., Ikeda, K. N., Lozano-Nunez, A., Anrather, D., Unterwurzacher, V.,**
913 **Gossenreiter, T., Perry, J. A., Crickley, R., Mercadante, C. J., Vaughan, S. et al.** (2015).
914 Proteomic identification of novel cytoskeletal proteins associated with TbPLK, an essential

915 regulator of cell morphogenesis in Trypanosoma brucei. *Molecular biology of the cell* **26**, 3013-
916 29.
917 **Morriswood, B., Havlicek, K., Demmel, L., Yavuz, S., Sealey-Cardona, M., Vidilaseris, K.,**
918 **Anrather, D., Kostan, J., Djinovic-Carugo, K., Roux, K. J. et al.** (2013). Novel Bilobe
919 Components in Trypanosoma brucei Identified Using Proximity-Dependent Biotinylation.
920 *Eukaryotic cell* **12**, 356-67.
921 **Morriswood, B., He, C. Y., Sealey-Cardona, M., Yelinek, J., Pypaert, M. and Warren, G.**
922 (2009). The bilobe structure of Trypanosoma brucei contains a MORN-repeat protein.
923 *Molecular and biochemical parasitology* **167**, 95-103.
924 **Morriswood, B. and Schmidt, K.** (2015). A MORN Repeat Protein Facilitates Protein Entry
925 into the Flagellar Pocket of Trypanosoma brucei. *Eukaryot Cell* **14**, 1081-93.
926 **Overath, P. and Engstler, M.** (2004). Endocytosis, membrane recycling and sorting of GPI-
927 anchored proteins: Trypanosoma brucei as a model system. *Mol Microbiol* **53**, 735-44.
928 **Perry, J. A., Sinclair-Davis, A. N., McAllaster, M. R. and de Graffenried, C. L.** (2018).
929 TbSmee1 regulates hook complex morphology and the rate of flagellar pocket uptake in
930 Trypanosoma brucei. *Mol Microbiol* **107**, 344-362.
931 **Postma, M. and Goedhart, J.** (2019). PlotsOfData-A web app for visualizing data together
932 with their summaries. *PLoS biology* **17**, e3000202.
933 **Price, H. P., Stark, M. and Smith, D. F.** (2007). Trypanosoma brucei ARF1 plays a central
934 role in endocytosis and golgi-lysosome trafficking. *Molecular biology of the cell* **18**, 864-73.
935 **Redmond, S., Vadivelu, J. and Field, M. C.** (2003). RNAit: an automated web-based tool for
936 the selection of RNAi targets in Trypanosoma brucei. *Molecular and biochemical parasitology*
937 **128**, 115-8.
938 **Schauberger, P.** (2021). openxlsx, pp. Simplifies the creation of Excel .xlsx files by providing
939 a
940 high level interface to writing, styling and editing worksheets.
941 Through the use of 'Rcpp', read/write times are comparable to the
942 'xlsx' and 'XLConnect' packages with the added benefit of removing the dependency on Java.
943 **Schindelin, J., Arganda-Carreras, I., Frise, E., Kaynig, V., Longair, M., Pietzsch, T.,**
944 **Preibisch, S., Rueden, C., Saalfeld, S., Schmid, B. et al.** (2012). Fiji: an open-source
945 platform for biological-image analysis. *Nat Methods* **9**, 676-82.
946 **Selvapandiyan, A., Kumar, P., Morris, J. C., Salisbury, J. L., Wang, C. C. and Nakhasi,**
947 **H. L.** (2007). Centrin1 is required for organelle segregation and cytokinesis in Trypanosoma
948 brucei. *Molecular biology of the cell* **18**, 3290-301.
949 **Shi, J., Franklin, J. B., Yelinek, J. T., Ebersberger, I., Warren, G. and He, C. Y.** (2008).
950 Centrin4 coordinates cell and nuclear division in T. brucei. *Journal of cell science* **121**, 3062-
951 70.

952 **Sunter, J. D. and Gull, K.** (2016). The Flagellum Attachment Zone: 'The Cellular Ruler' of
953 Trypanosome Morphology. *Trends Parasitol* **32**, 309-324.
954 **Sunter, J. D., Varga, V., Dean, S. and Gull, K.** (2015). A dynamic coordination of flagellum
955 and cytoplasmic cytoskeleton assembly specifies cell morphogenesis in trypanosomes.
956 *Journal of cell science* **128**, 1580-94.
957 **Team, R. C.** (2021). R: A Language and Environment for Statistical Computing.
958 **Watson, J. F. and Garcia-Nafria, J.** (2019). In vivo DNA assembly using common laboratory
959 bacteria: A re-emerging tool to simplify molecular cloning. *J Biol Chem* **294**, 15271-15281.
960 **Wirtz, E., Leal, S., Ochatt, C. and Cross, G. A.** (1999). A tightly regulated inducible
961 expression system for conditional gene knock-outs and dominant-negative genetics in
962 Trypanosoma brucei. *Molecular and biochemical parasitology* **99**, 89-101.
963 **Woods, A., Baines, A. J. and Gull, K.** (1989). Evidence for a Mr 88,000 glycoprotein with a
964 transmembrane association to a unique flagellum attachment region in Trypanosoma brucei.
965 *Journal of cell science* **93 (Pt 3)**, 501-8.
966 **Zhou, Q., Gheiratmand, L., Chen, Y., Lim, T. K., Zhang, J., Li, S., Xia, N., Liu, B., Lin, Q.**
967 **and He, C. Y.** (2010). A comparative proteomic analysis reveals a new bi-lobe protein required
968 for bi-lobe duplication and cell division in Trypanosoma brucei. *PloS one* **5**, e9660.
969 **Zhou, Q., Hu, H., He, C. Y. and Li, Z.** (2015). Assembly and maintenance of the flagellum
970 attachment zone filament in Trypanosoma brucei. *Journal of cell science* **128**, 2361-72.
971 **Zoltner, M., Leung, K. F., Alsford, S., Horn, D. and Field, M. C.** (2015). Modulation of the
972 Surface Proteome through Multiple Ubiquitylation Pathways in African Trypanosomes. *PLoS*
973 *Pathog* **11**, e1005236.
974
975
976
977 **Figure legends**
978
979 **Figure 1. TbSmee1 is a cytoskeleton-associated phosphoprotein.** (A) Schematic
980 representation of TbSmee1 (766 amino acids long) with the three predicted domains shown
981 in purple, orange, and teal. Approximate amino acid ranges of each domain are indicated. The
982 regions used as antigens for the generation of the three anti-TbSmee1 antibodies (303, 304,
983 508) are shown in light and dark green bars below the schematic. (B) Validation of the
984 specificity of the three anti-TbSmee1 antibodies. Immunoblots were carried out against whole
985 cell lysates from uninduced TbSmee1 RNAi cells (Tet -), induced TbSmee1 RNAi cells (Tet
986 +), and Ty1-TbSmee1 endogenous replacement cells (End. repl.) using the three anti-
987 TbSmee1 antibodies (304, 303, 508). All three antibodies detected an ~ 80 kDa protein in the
988 Tet - samples (upper panels). The protein was strongly depleted after induction of TbSmee1

989 RNAi (Tet +). A second heavier band was detected in the endogenous replacement cells. This
990 heavier band could also be detected using anti-Ty1 (BB2) antibodies (lower panels).
991 Exemplary results from multiple (n>3) independent experiments are shown. (C) Fractionation
992 scheme. Bloodstream form (BSF) cells were extracted with the non-ionic detergent IGEPAL
993 and separated into cytoplasm and cytoskeleton fractions by centrifugation. (D) TbSmee1 is
994 associated with the cytoskeleton. Immunoblot of whole-cell input (I), cytoplasmic supernatant
995 (SN) and cytoskeletal pellet (P) fractions with anti-TbSmee1 antibodies. Equal fractions were
996 loaded in each lane. Exemplary results from multiple (n>3) experiments are shown. (E)
997 TbSmee1 is phosphorylated in vivo. Trypanosome cells were lysed and the lysates incubated
998 with λ phosphatase for the indicated times (0-20 min), followed by TbSmee1 detection by
999 immunoblotting. The fuzzy appearance of the TbSmee1 was gradually lost over the
1000 timecourse. This was not observed if the lysates were kept in the presence of phosphatase
1001 inhibitors (+ inhibit), either at 24 ºC or on ice. Equal loading of samples was confirmed using
1002 total protein stain (magenta). Exemplary results from multiple (n>3) independent experiments
1003 are shown. (F) TbSmee1 localisation through the cell cycle. Bloodstream form trypanosomes
1004 were extracted using non-ionic detergent, fixed, and labelled with anti-TbSmee1 antibodies.
1005 DNA was stained using DAPI. In 1K1N cells, TbSmee1 localised to a bar-shaped structure
1006 (arrow) close to the kinetoplast. In 2K1N cells the structure had replicated (arrows). TbSmee1
1007 was additionally present on a third structure farther along the cell body (arrowhead). In 2K2N
1008 cells the signal intensity of the third structure was much weaker. Exemplary images from
1009 multiple (n>3) independent experiments are shown.
1010
1011 **Figure 2. TbSmee1 is localised to the shank part of the hook complex.** Bloodstream form
1012 trypanosomes were extracted with non-ionic detergent, fixed, and labelled with the indicated
1013 antibodies. Either wild-type or Ty1-TbSmee1 cells were used. Correlation plots are shown
1014 next to the immunofluorescence data. (A) TbSmee1 overlaps with the shank part of the hook
1015 complex protein TbMORN1 (arrow). (B) TbSmee1 overlaps with the shank part of the hook
1016 complex protein TbLRRP1 (arrow). (C) TbSmee1 partially overlaps with TbCen4. TbCen4 is
1017 present at the basal and probasal bodies (yellow arrow), centrin arm (arrowhead), and a small
1018 additional projection (white arrow). (D) TbSmee1 does not overlap with the flagellar pocket
1019 collar protein TbBILBO1 (arrow). (E) Summary of measured correlation coefficients for each
1020 of the colabelling experiments. Each dot represents a single cell. All fluorescence images are
1021 maximum intensity projections, and an overlay with a single DIC section is shown. Overlap
1022 was manually confirmed in single z-slices. Results were obtained from multiple (n>3)
1023 independent experiments; exemplary images are shown.
1024

1025 **Figure 3. TbSmee1 is associated with the tip of the elongating new FAZ in replicating**
1026 **cells.** (A) Bloodstream form trypanosomes were extracted with non-ionic detergent, fixed, and
1027 labelled with the indicated antibodies. DNA was stained with DAPI. Maximum intensity
1028 projections are shown, with a single DIC z-slice overlaid. In 1K1N cells, TbSmee1 partially
1029 overlapped (arrow) with the posterior end of the FAZ. In 2K1N and 2K2N cells, the additional
1030 TbSmee1 structure (arrowhead) was present at the tip of the elongating new FAZ. Exemplary
1031 images from multiple (n>3) independent experiments are shown. (B) SIM image of the same
1032 preparations. The TbSmee1 structure (inset) lay just ahead of the elongating FAZ tip. (C) SIM
1033 image of a detergent-extracted cell colabelled for TbSmee1 and TbDOT1. TbDOT1 appeared
1034 to envelop and partially overlap with TbSmee1.
1035
1036 **Figure 4. TbSmee1 domains 2 and 3 are required for targeting to the hook complex.** (A)
1037 Schematics of the 9 TbSmee1 truncation constructs tested, along with details of amino acid
1038 ranges, localisation, and size in kDa. (B) TbSmee1 domains 2 and 3 are required for
1039 localisation to the hook complex. Stably-transfected cells that inducibly expressed the
1040 indicated TbSmee1 truncations were used. Ty1-TbSmee1 was detected using anti-Ty1
1041 antibodies. In the absence of induction (-Tet), no signal overlapping with endogenous
1042 TbMORN1 was seen. After induction of expression (+Tet), the Ty1-TbSmee1 truncations
1043 overlapped with the shank part of TbMORN1 (insets). Images shown are maximum intensity
1044 projections of the fluorescence channels overlaid with a single DIC z-slice. Exemplary images
1045 are shown. (C) Confirmation of Ty1-TbSmee1 truncation expression. Whole-cell lysates from
1046 control (-Tet) cells and cells expressing Ty1-TbSmee1 truncations (+Tet) were immunoblotted
1047 using anti-TbSmee1 (left panel) and anti-Ty1 (right panel) antibodies. Total protein stain was
1048 used for normalisation. In the exemplary blot shown, the Ty1-TbSmee1 was detected at ~ 44
1049 kDa, as expected. (D) Quantification of immunoblotting data. Anti-TbSmee1 signals in the
1050 immunoblots were normalised relative to total protein staining. TbSmee1 levels in control (T-)
1051 cells were expressed relative to the mean value of all control samples. Ty1-TbSmee1 levels
1052 were expressed relative to the levels of endogenous TbSmee1 in each clone. All data in the
1053 experiments shown in this figure were obtained from two independent experiments with each
1054 Ty1-TbSmee1 truncation; each experiment used three separate clones.
1055
1056 **Figure 5. TbSmee1 is essential for the viability of bloodstream form *T. brucei*.** (A)
1057 Depletion of TbSmee1 causes a strong growth defect. The population density of uninduced
1058 control (Tet-) and TbSmee1-depleted (Tet+) cells were measured at regular intervals after
1059 induction of RNAi over a 72 h timecourse. The insert shows data from a more high-resolution
1060 experiments with readings taken at hourly intervals. A growth defect was evident from 21 h
1061 post-induction onwards. (B) Confirmation of TbSmee1 depletion at the single-cell level.

1062 Uninduced control (Tet-) and TbSmee1-depleted (Tet+) RNAi cells were extracted, fixed, and
1063 labelled with anti-TbSmee1 antibodies (green). DNA was labelled with DAPI (magenta).
1064 Maximum intensity projections of the fluorescence channels are shown overlaid with a single
1065 DIC z-slice. Insets show the TbSmee1 signal. Exemplary 1K1N and 2K2N cells from each
1066 condition are shown. (C) Confirmation and quantification of TbSmee1 depletion. Whole-cell
1067 lysates from control (Tet-) and TbSmee1-depleted (Tet+) RNAi cells were immunoblotted
1068 using antibodies against TbSmee1 (green). Total protein stain (TPS, magenta) was used for
1069 signal normalisation. An exemplary immunoblot is shown. Normalised TbSmee1 signals in
1070 +Tet cells were expressed relative to the -Tet signal for each sample. TbSmee1 -Tet signals
1071 were expressed relative to the mean of all TbSmee1 -Tet values in the dataset. TbSmee1
1072 depletion was quantified at the indicated timepoints post-induction. (D) Depletion of TbSmee1
1073 results in an enlargement of the flagellar pocket. Electron microscopy images of control (Tet-
1074) and TbSmee1-depleted (Tet+) RNAi cells are shown. The cells were fixed 24 h post-
1075 induction. All data in the experiments shown in this figure were obtained from multiple (n≥3)
1076 independent experiments, each using three separate clones.
1077
1078 **Figure 6. Flagellar pocket enlargement is an early consequence of TbSmee1 depletion.**
1079 (A) Summary of dextran uptake protocol. The use of temperature blocks inhibits endocytosis,
1080 allowing dextran to enter the flagellar pocket but not be internalised. (B) The intensity of the
1081 dextran signal reports on flagellar pocket volume. Cells were incubated with fluorophore-
1082 conjugated dextran (green) prior to being fixed and imaged using fluorescence microscopy.
1083 DNA was labelled with DAPI (magenta). Exemplary cells from control (- Tet) and TbSmee1-
1084 depleted (+ Tet) conditions are shown. The + Tet cells exhibited various degrees of flagellar
1085 pocket enlargement and progressive morphological aberration. Insets show the dextran signal
1086 with a log-scale LUT. (C) Flow cytometry analysis of control (- Tet) and TbSmee1-depleted (+
1087 Tet) cells incubated with fluorescent dextran at various timepoints after induction of RNAi. At
1088 later timepoints there is a clear emergence of a subpopulation of cells with much greater
1089 fluorescence intensity (arrow). Exemplary traces from a single experiment are shown. (D)
1090 Quantification of flow cytometry data. The geometric mean of the fluorescence intensity in
1091 control (- Tet) and TbSmee1-depleted (+ Tet) cells was measured at various timepoints after
1092 induction of RNAi. Bars indicate median values. The population mean of the + Tet cells was
1093 clearly higher at the later timepoints; a visible shift was visible as early as 18 h post-induction
1094 (arrow). All data in the experiments shown in this figure were obtained from multiple (n≥2)
1095 independent experiments; each experiment used three separate clones.
1096
1097 **Figure 7. Surface-bound reporters cannot enter the flagellar pocket of TbSmee1-**
1098 **depleted cells.** (A) Summary of paired dextran+ConA uptake protocol. (B) ConA is unable to

1099 enter the enlarged flagellar pocket of TbSmee1-depleted cells. In control (-Tet) cells, the
1100 dextran and ConA signals strongly overlapped (arrow, upper panels). In TbSmee1-depleted
1101 cells (+Tet), little to no overlap between the two reporters was observed (arrow, lower panels).
1102 Maximum intensity projections of the fluorescence channels are shown overlaid with a single
1103 DIC z-slice. (C) Quantification of dextran+ConA uptake experiments. Cells from control (-Tet)
1104 and TbSmee1-depleted (+Tet) samples were manually classified into four categories (1-4)
1105 based on the degree of overlap between the ConA and dextran reporters. Results are shown
1106 as a slope chart (left) and stacked bar chart (right); exemplary cells for each category are
1107 shown. (D) Summary of paired dextran+BSA uptake protocol. (E) BSA is unable to enter the
1108 enlarged flagellar pocket of TbSmee1-depleted cells. (F) Quantification of dextran+BSA
1109 uptake experiments. Data were obtained from multiple (n>3) independent experiments; each
1110 experiment used three separate clones.
1111
1112 **Figure 8. Blockade of surface reporters is due to an inhibition of endocytosis.** (A)
1113 Summary of paired dextran+ConA uptake protocol. (B) ConA is unable to enter the enlarged
1114 flagellar pocket of clathrin-depleted cells. In control (-Tet) cells, the dextran and ConA signals
1115 strongly overlapped (arrow, upper panels). In clathrin-depleted cells (+Tet), little to no overlap
1116 between the two reporters was observed (arrow, lower-panels). Maximum intensity projections
1117 of the fluorescence channels are shown overlaid with a single DIC z-slice. (C) Quantification
1118 of dextran+ConA uptake experiments. Cells from control (-Tet) and clathrin-depleted (+Tet)
1119 samples were manually classified into four categories (1-4) based on the degree of overlap
1120 between the ConA and dextran reporters. Results are shown as a slope chart (left) and
1121 stacked bar chart (right); exemplary cells for each category are shown. (D) Summary of paired
1122 dextran+BSA uptake protocol. (E) BSA is unable to enter the enlarged flagellar pocket of
1123 clathrin-depleted cells. (F) Quantification of dextran+BSA uptake experiments. Data were
1124 obtained from multiple (n>3) independent experiments; each experiment used three separate
1125 clones.
1126
1127
1128 **Figure S1. The TbSmee1 primary structure contains three blocks of highly-conserved**
1129 **sequence.** Multiple sequence alignment of *Trypanosoma brucei* Smee1 (TbSmee1) and
1130 homologous proteins from other trypanosome species, generated using MultAlin (Corpet,
1131 1988) with default parameters. Amino acid numbers are indicated in black numerals above
1132 the alignment. Moderately (50-90%) conserved residues are highlighted in blue. Highly-
1133 conserved (>90%) or completely conserved residues are highlighted in red. The consensus
1134 sequence is shown below the alignment. Abbreviations: TbSmee1, *Trypanosoma brucei*
1135 Smee1; T.cong, *Trypanosoma congolense*; T.vivax, *Trypanosoma vivax*; T.grayi,

1136 *Trypanosoma grayi*. T.conorhini, *Trypanosoma conorhini*; T.rangelii, *Trypanosoma rangelii*;
1137 T.cruzi, *Trypanosoma cruzi*; T.theileri, *Trypanosoma theileri*. The % sequence identity of each
1138 homologue to TbSmee1 is indicated after the name.
1139
1140 **Figure S2. TbSmee1 contains three predicted structured domains.** (A) Schematic
1141 representation of TbSmee1 with the three predicted domains (Dom1/2/3) indicated in blue,
1142 magenta, and green. The approximate amino acid coordinates in the primary structure are
1143 indicated in black above each domain. The isoelectric point (pI) of each domain is indicated in
1144 bold text above the domain. (B) TbSmee1 contains three regions of predicted secondary
1145 structure. Secondary structure prediction generated using the PSIPRED server (Buchan &
1146 Jones, 2019) with default parameters. Abbreviations and schematics are defined in the legend
1147 at the bottom right. The three predicted structured domains are outlined as blue, magenta,
1148 and green boxes.
1149
1150 **Figure S3. Generation of Ty1-TbSmee1 endogenous replacement cell line.** (A) Schematic
1151 showing the in situ tagging procedure and annealing sites for PCR primers. The two
1152 endogenous alleles of TbSmee1 in the gDNA are shown in yellow, flanked by 5'UTR and
1153 3'UTR sequences. *T.* brucei cells were transfected with a targeting fragment with homology
1154 arms for recombination with the 3' end of the 5'UTR and 5' end of the ORF. The targeting
1155 fragment contained a blasticidin resistance gene (bla^R), the intergenic region from the
1156 alpha/beta tubulin locus ($\alpha\beta$) and a 3xTy1 epitope tag preceded by an ATG start codon.
1157 Homologous recombination removed the endogenous ATG start codon of the TbSmee1 ORF.
1158 (B) Confirmation of targeting fragment integration at the endogenous TbSmee1 locus by PCR
1159 analysis of genomic DNA. Genomic DNA from wild-type (wt) and candidate Ty1-TbSmee1
1160 clones (c1,c2,c3) was analysed by PCR. Left panel: positive control using 8820_ORF_F and
1161 8820_gDNA-R primers; 490 bp product expected. Right panel: integration test using BB2-F
1162 and 8820_gDNA-R primers. A product is only expected if the 3xTy1 sequence has integrated
1163 upstream of the TbSmee1 ORF (see primer annealing sites in panel A). Two independent
1164 experiments were carried out, each using all three separate clones. (C) Ty1-TbSmee1
1165 displays the same localisations through the cell cycle as endogenous TbSmee1. Detergent-
1166 extracted cells were fixed with methanol and labelled with anti-Ty1 antibodies; DAPI was
1167 stained using DAPI. Exemplary cells from the three main cell cycle states (1K1N, 2K1N, 2K2N)
1168 are shown. Maximum-intensity z-projections of the fluorescence channels are shown, together
1169 with a single DIC z-slice overlay. The Ty1-TbSmee1 signal is shown in magenta in the overlay
1170 and highlighted with arrows. Arrowheads indicate the Ty1-TbSmee1 present at the tip of the
1171 new FAZ. Insets show an enlarged view of the TbSmee1 signal from the hook complex or FAZ
1172 tip. Multiple (n>3) independent experiments were carried out using three separate clones. (D)

1173 The anti-Ty1 signal is specific for Ty1-TbSmee1. Wild-type (wt) and a Ty1-TbSmee1 clone
1174 (c1) were extracted with detergent, fixed with methanol, and labelled with anti-TbSmee1 and
1175 anti-Ty1 antibodies. Hook complex (arrows) and FAZ tip (arrowheads) localisations are
1176 indicated. No anti-Ty1 signal was seen in wild-type cells; strong overlap between the anti-Ty1
1177 and anti-TbSmee1 signals was seen in the Ty1-TbSmee1 cells. Maximum-intensity z-
1178 projections of the fluorescence channels are shown, together with a single DIC z-slice overlay.
1179
1180 **Figure S4. Validation of anti-TbStarkey1 antibodies.** (A) Validation of anti-TbStarkey1
1181 antibody specificity by immunoblotting. Three separate TbStarkey1 RNAi clones (c8, c9, c10)
1182 were analysed by immunoblotting. Both whole-cell lysates (WCL) and detergent-extracted
1183 cytoskeleton (CK) samples were obtained at the indicated timepoints (24 h, 48 h) from control
1184 (Tet-) and induced (Tet+) cells. The samples were immunoblotted using two separate anti-
1185 TbStarkey1 affinity-purified antibodies (antibody 476, 477). Both antibodies recognised a >130
1186 kDa protein whose abundance was depleted after 48 h of RNAi. The 476 antibody additionally
1187 showed a significant cross-reaction with a protein of <100 kDa in WCL but not CK samples. A
1188 section of the total protein stain of each membrane is shown as an inset (magenta). (B)
1189 Validation of anti-TbStarkey1 antibody specificity by immunofluorescence microscopy. Control
1190 (Tet-) and TbStarkey1-depleted (Tet+) RNAi cells were extracted with nonionic detergent,
1191 fixed with methanol, and labelled with anti-TbStarkey1 antibodies (green); DNA was stained
1192 using DAPI (magenta). TbStarkey1 localised to the hook complex, and signal was lost upon
1193 depletion. The boxed areas are shown enlarged in the bottom panels. Identical results were
1194 obtained using both anti-TbStarkey1 antibodies; exemplary images using the 477 antibodies
1195 are shown. (C) TbSmee1 overlaps with the shank part of the hook complex protein TbStarkey1
1196 (arrow). (D) The TbSmee1 and TbStarkey1 pixel values are correlated. (E) Summary of
1197 measured correlation coefficients. Each dot represents a single cell. All fluorescence images
1198 are maximum intensity projections, and an overlay with a single DIC section is shown. Overlap
1199 was manually confirmed in single z-slices. Results were obtained from multiple (n>3)
1200 independent experiments; exemplary images are shown.
1201
1202
1203 **Figure S5. Validation of TbSmee1 truncations.** (A) Validation of Ty1-TbSmee1 truncation
1204 cell lines by PCR analysis of genomic DNA and immunoblotting. The results for all 8 TbSmee1
1205 truncations are shown, separated by dotted lines. Upper panels: PCR analysis of genomic
1206 DNA to confirm the presence of the truncation construct. PCR was used to amplify DNA from
1207 clones (c1, c2, c3) and wild-type control (wt) genomic DNA. Primers annealing to the sequence
1208 encoding Ty1 epitope and within the truncation were used. Lower panels: confirmation of Ty1-
1209 TbSmee1 truncation construct expression by immunoblotting. Whole-cell lysates from

1210 uninduced (-Tet) and induced (+Tet) cells were analysed by immunoblotting with anti-
1211 TbSmee1 (green) and anti-Ty1 (cyan) antibodies. Both antibodies detected proteins
1212 corresponding to the predicted size of the Ty1-TbSmee1 truncations; arrows indicate the
1213 target protein in the anti-Ty1 blots. A portion of the total protein staining of the membranes is
1214 shown in magenta. (B) Ty1-TbSmee1(161-766) localises to both the hook complex and the
1215 FAZ tip. Cells expressing the Ty1-TbSmee1(161-766) construct were extracted with nonionic
1216 detergent, fixed with methanol, and labelled with anti-TbMORN1 and anti-Ty1 antibodies. DNA
1217 was stained with DAPI (cyan). Ty1-TbSmee1(161-766) was observed at both the hook
1218 complex and the FAZ tip (arrow). (C) Ty1-TbSmee1(2-400) localises to the FAZ tip but not the
1219 hook complex. Cells expressing the Ty1-TbSmee1(2-400) construct were extracted, fixed, and
1220 labelled as above. Ty1-TbSmee1(2-400) was observed exclusively at the FAZ tip (arrow).
1221 Images in panels B and C are maximum intensity z-projections with a single DIC z-slice
1222 overlay. Multiple (n>2) independent experiments using three separate clones for each
1223 construct were carried out; exemplary cells are shown.
1224
1225 **Figure S6. Additional results for TbSmee1 and TbStarkey1 RNAi experiments.** (A)
1226 TbSmee1 depletion causes changes to cell cycle state distribution. Control (Tet-) and
1227 TbSmee1-depleted (Tet+) RNAi cells from 18 h, 21 h, 24 h post-induction were fixed using
1228 glutaraldehyde; DNA was stained using DAPI. The various cell cycle states (1K1N, etc) were
1229 manually quantified from images taken of the fixed cells. Data were obtained from three
1230 independent experiments, each using three separate clones; at least 240 cells were quantified
1231 for each timepoint. (B) Depletion of TbStarkey1 has no effect on population cell growth. Control
1232 (-Tet) and TbStarkey1-depleted (+Tet) cells were followed over a 72 h timecourse, and
1233 population density (cells/ml) was measured every 24 h. Data were obtained from three
1234 independent experiments, each using 3 separate clones. (C, D) Depletion of TbStarkey1
1235 causes morphological abnormality. TbStarkey1-depleted cells were prepared for electron
1236 microscopy using high-pressure freezing and imaged. Cells with enlarged flagellar pockets
1237 could readily be observed.
1238
1239 **Figure S7. Depletion of TbSmee1 affects other cytoskeleton-associated proteins.**
1240 TbSmee1 RNAi cells were induced for 24 h and analysed by immunoblotting of whole-cell
1241 lysates and immunofluorescence imaging of detergent-extracted cells. (A) Exemplary
1242 immunoblots showing the effect of 24 h TbSmee1 depletion on marker proteins for the hook
1243 complex, flagellar pocket collar, and centrin arm. For comparison, the effect of 16 h TbMORN1
1244 depletion was also analysed. (B) Quantification of immunoblot data. TbSmee1 depletion did
1245 not affect any of the proteins analysed. Total protein staining was used for signal
1246 normalisation. Normalised TbSmee1 signals in +Tet cells were expressed relative to the -Tet

1247 signal for each sample. TbSmee1 -Tet signals were expressed relative to the mean of all
1248 TbSmee1 -Tet values in the dataset. Immunoblots from TbMORN1 RNAi experiments were
1249 quantified in the same way; TbMORN1 depletion resulted in a loss of both TbSmee1 and
1250 TbStarkey1 signal. Data were obtained from multiple (n>2) independent experiments, each
1251 using three (TbSmee1 RNAi) or two (TbMORN1 RNAi) separate clones. (C-F) TbSmee1
1252 depletion affects TbLRRP1 but not other marker proteins analysed. Control (-Tet) and
1253 TbSmee1-depleted (+Tet) cells were extracted with detergent, fixed with methanol, and
1254 labelled with the indicated antibodies; DNA was stained using DAPI. The position of the hook
1255 complexes in exemplary 1K1N and 2K2N cells are shown with arrows; panel E also indicates
1256 basal bodies. Data were obtained from 2 independent experiments for each labelling
1257 combination, each using 3 separate clones. (G) TbSmee1 and TbLRRP1 in TbMORN1-
1258 depleted cells. (H) Summary of the observed effects on the abundance of marker proteins
1259 caused by either TbMORN1 or TbSmee1 depletion, based on immunoblotting and
1260 immunofluorescence data.
1261
1262
1263 **Figure S8. Depletion of TbSmee1 prevents trafficking of ConA to the lysosome.** Control
1264 (-Tet) and TbSmee1-depleted cells (+Tet; 24 h timepoint) were incubated on ice with ConA
1265 (magenta). The cells were then shifted to 37 ºC for 30 min to allow internalisation. The cells
1266 were then fixed and labelled with antibodies specific for the lysosome marker p67 (green).
1267 Control (-Tet) cells showed strong overlap between the two labels, indicating that ConA had
1268 been trafficked to the lysosome. +Tet cells showed no overlap between the two labels.
1269 Maximum intensity projections of the fluorescence channels are shown overlaid with a single
1270 DIC z-slice. Overlap in -Tet cells was confirmed in single z-slices. Single channels from the
1271 boxed area in each image are shown as insets. Data obtained from multiple (n>2) independent
1272 experiments each using three separate clones; exemplary cells are shown.
1273
1274
1275
1276
1277

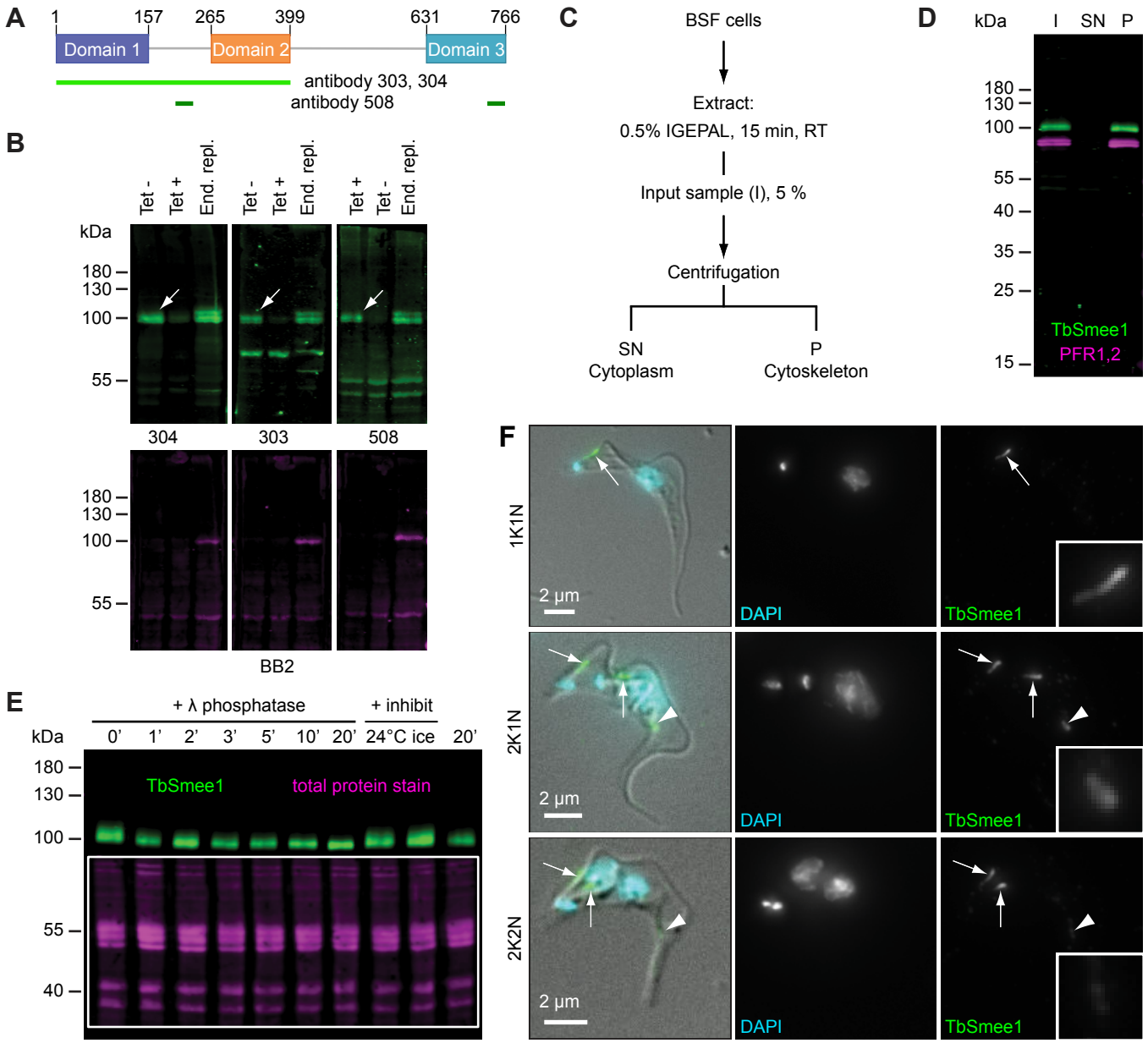

Figure 1. TbSmee1 is a cytoskeleton-associated phosphoprotein. (A) Schematic representation of TbSmee1 (766 amino acids long) with the three predicted domains shown in purple, orange, and teal. Approximate amino acid ranges of each domain are indicated. The regions used as antigens for the generation of the three anti-TbSmee1 antibodies (303, 304, 508) are shown in light and dark green bars below the schematic. (B) Validation of the specificity of the three anti-TbSmee1 antibodies. Immunoblots were carried out against whole cell lysates from uninduced TbSmee1 RNAi cells (Tet -), induced TbSmee1 RNAi cells (Tet +), and Ty1-TbSmee1 endogenous replacement cells (End. repl.) using the three anti-TbSmee1 antibodies (304, 303, 508). All three antibodies detected an ~ 80 kDa protein in the Tet - samples (upper panels). The protein was strongly depleted after induction of TbSmee1 RNAi (Tet +). A second heavier band was detected in the endogenous replacement cells. This heavier band could also be detected using anti-Ty1 (BB2) antibodies (lower panels). Exemplary results from multiple (n>3) independent experiments are shown. (C) Fractionation scheme. Bloodstream form (BSF) cells were extracted with the non-ionic detergent IGEPAL and separated into cytoplasm and cytoskeleton fractions by centrifugation. (D) TbSmee1 is associated with the cytoskeleton. Immunoblot of whole-cell input (I), cytoplasmic supernatant (SN) and cytoskeletal pellet (P) fractions with anti-TbSmee1 antibodies. Equal fractions were loaded in each lane. Exemplary results from multiple (n>3) experiments are shown. (E) TbSmee1 is phosphorylated in vivo. Trypanosome cells were lysed and the lysates incubated with λ phosphatase for the indicated times (0-20 min), followed by TbSmee1 detection by immunoblotting. The fuzzy appearance of the TbSmee1 was gradually lost over the timecourse. This was not observed if the lysates were kept in the presence of phosphatase inhibitors (+ inhibit), either at 24 ºC or on ice. Equal loading of samples was confirmed using total protein stain (magenta). Exemplary results from multiple (n>3) independent experiments are shown. (F) TbSmee1 localisation through the cell cycle. Bloodstream form trypanosomes were extracted using non-ionic detergent, fixed, and labelled with anti-TbSmee1 antibodies. DNA was stained using DAPI. In 1K1N cells, TbSmee1 localised to a bar-shaped structure (arrow) close to the kinetoplast. In 2K1N cells the structure had replicated (arrows). TbSmee1 was additionally present on a third structure farther along the cell body (arrowhead). In 2K2N cells the signal intensity of the third structure was much weaker. Exemplary images from multiple (n>3) independent experiments are shown.

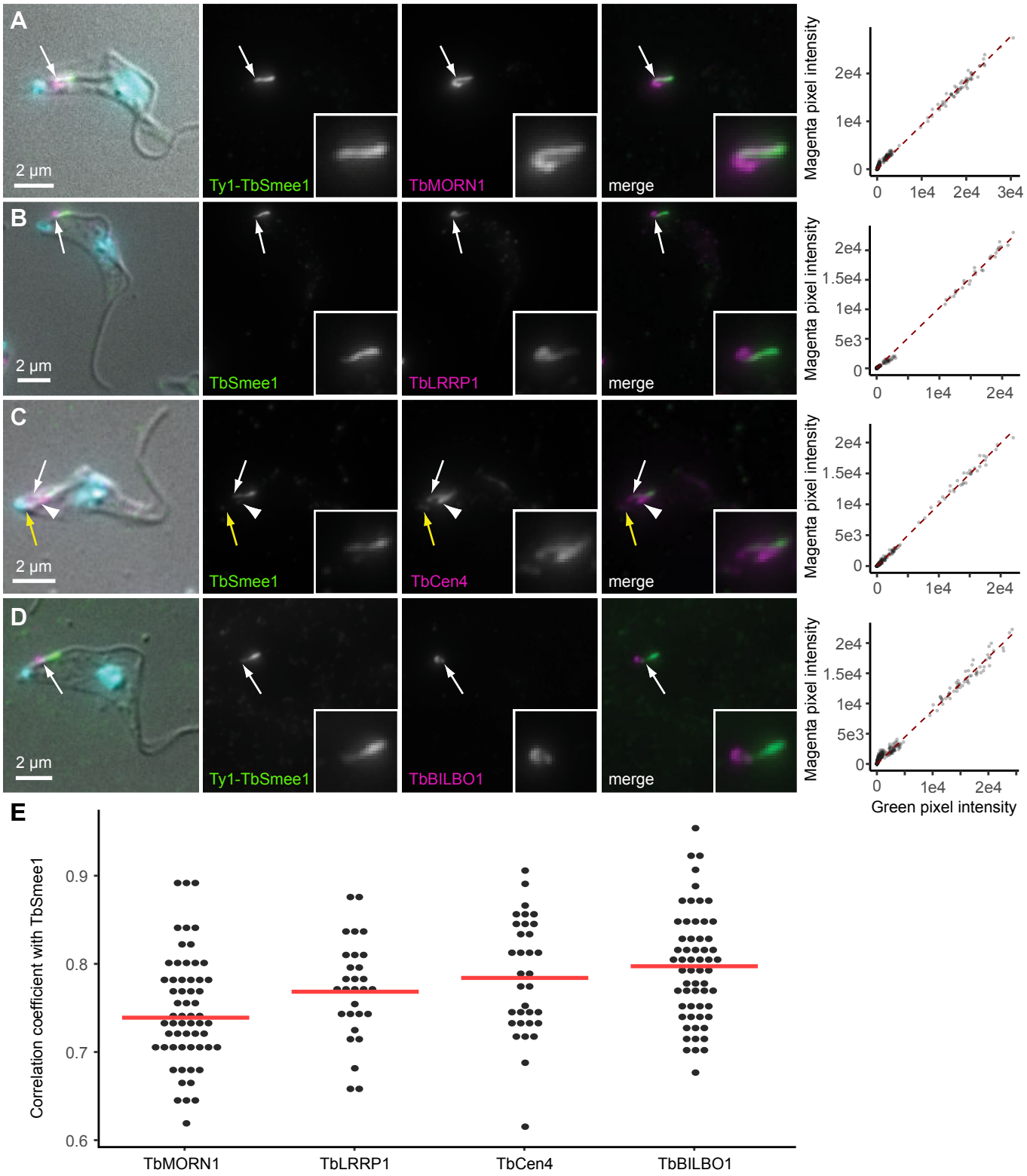

Figure 2. TbSmee1 is localised to the shank part of the hook complex. Bloodstream form trypanosomes were extracted with non-ionic detergent, fixed, and labelled with the indicated antibodies. Either wild-type or Ty1-TbSmee1 cells were used. Correlation plots are shown next to the immunofluorescence data. (A) TbSmee1 overlaps with the shank part of the hook complex protein TbMORN1 (arrow). (B) TbSmee1 overlaps with the shank part of the hook complex protein TbLRRP1 (arrow). (C) TbSmee1 partially overlaps with TbCen4. TbCen4 is present at the basal and probasal bodies (yellow arrow), centrin arm (arrowhead), and a small additional projection (white arrow). (D) TbSmee1 does not overlap with the flagellar pocket collar protein TbBILBO1 (arrow). (E) Summary of measured correlation coefficients for each of the colabelling experiments. Each dot represents a single cell. All fluorescence images are maximum intensity projections, and an overlay with a single DIC section is shown. Overlap was manually confirmed in single z-slices. Results were obtained from multiple (n>3) independent experiments; exemplary images are shown.

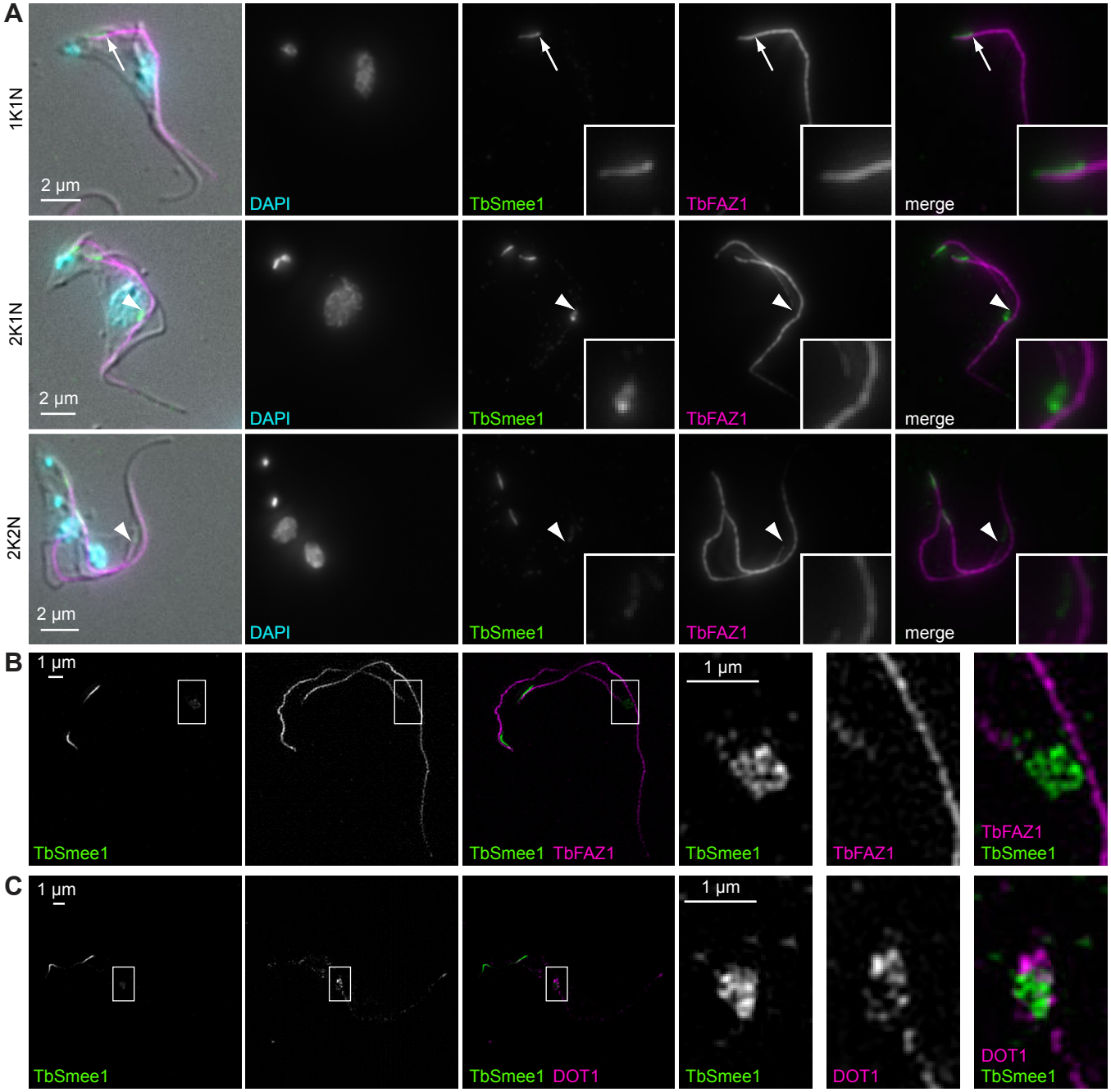

Figure 3. TbSmee1 is associated with the tip of the elongating new FAZ in replicating cells. (A) Bloodstream form trypanosomes were extracted with non-ionic detergent, fixed, and labelled with the indicated antibodies. DNA was stained with DAPI. Maximum intensity projections are shown, with a single DIC z-slice overlaid. In 1K1N cells, TbSmee1 partially overlapped (arrow) with the posterior end of the FAZ. In 2K1N and 2K2N cells, the additional TbSmee1 structure (arrowhead) was present at the tip of the elongating new FAZ. Exemplary images from multiple (n>3) independent experiments are shown. (B) SIM image of the same preparations. The TbSmee1 structure (inset) lay just ahead of the elongating FAZ tip. (C) SIM image of a detergent-extracted cell colabelled for TbSmee1 and TbDOT1. TbDOT1 appeared to envelop and partially overlap with TbSmee1.

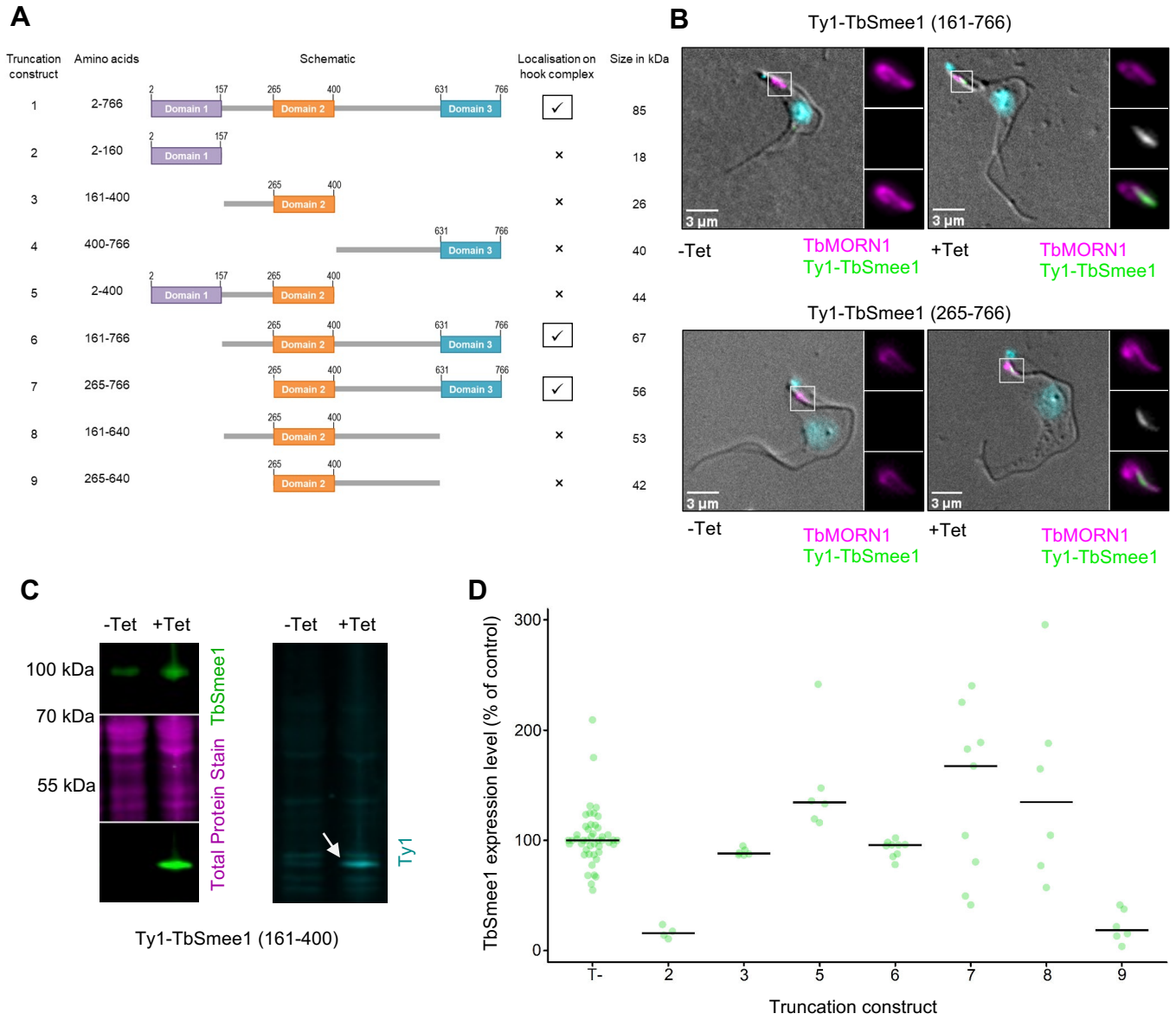

Figure 4. TbSmee1 domains 2 and 3 are required for targeting to the hook complex. (A) Schematics of the 9 TbSmee1 truncation constructs tested, along with details of amino acid ranges, localisation, and size in kDa. (B) TbSmee1 domains 2 and 3 are required for localisation to the hook complex. Stably-transfected cells that inducibly expressed the indicated TbSmee1 truncations were used. Ty1-TbSmee1 was detected using anti-Ty1 antibodies. In the absence of induction (-Tet), no signal overlapping with endogenous TbMORN1 was seen. After induction of expression (+Tet), the Ty1-TbSmee1 truncations overlapped with the shank part of TbMORN1 (insets). Images shown are maximum intensity projections of the fluorescence channels overlaid with a single DIC z-slice. Exemplary images are shown. (C) Confirmation of Ty1-TbSmee1 truncation expression. Whole-cell lysates from control (-Tet) cells and cells expressing Ty1-TbSmee1 truncations (+Tet) were immunoblotted using anti-TbSmee1 (left panel) and anti-Ty1 (right panel) antibodies. Total protein stain was used for normalisation. In the exemplary blot shown, the Ty1-TbSmee1 was detected at ~ 44 kDa, as expected. (D) Quantification of immunoblotting data. Anti-TbSmee1 signals in the immunoblots were normalised relative to total protein staining. TbSmee1 levels in control (T-) cells were expressed relative to the mean value of all control samples. Ty1-TbSmee1 levels were expressed relative to the levels of endogenous TbSmee1 in each clone. All data in the experiments shown in this figure were obtained from two independent experiments with each Ty1-TbSmee1 truncation; each experiment used three separate clones.

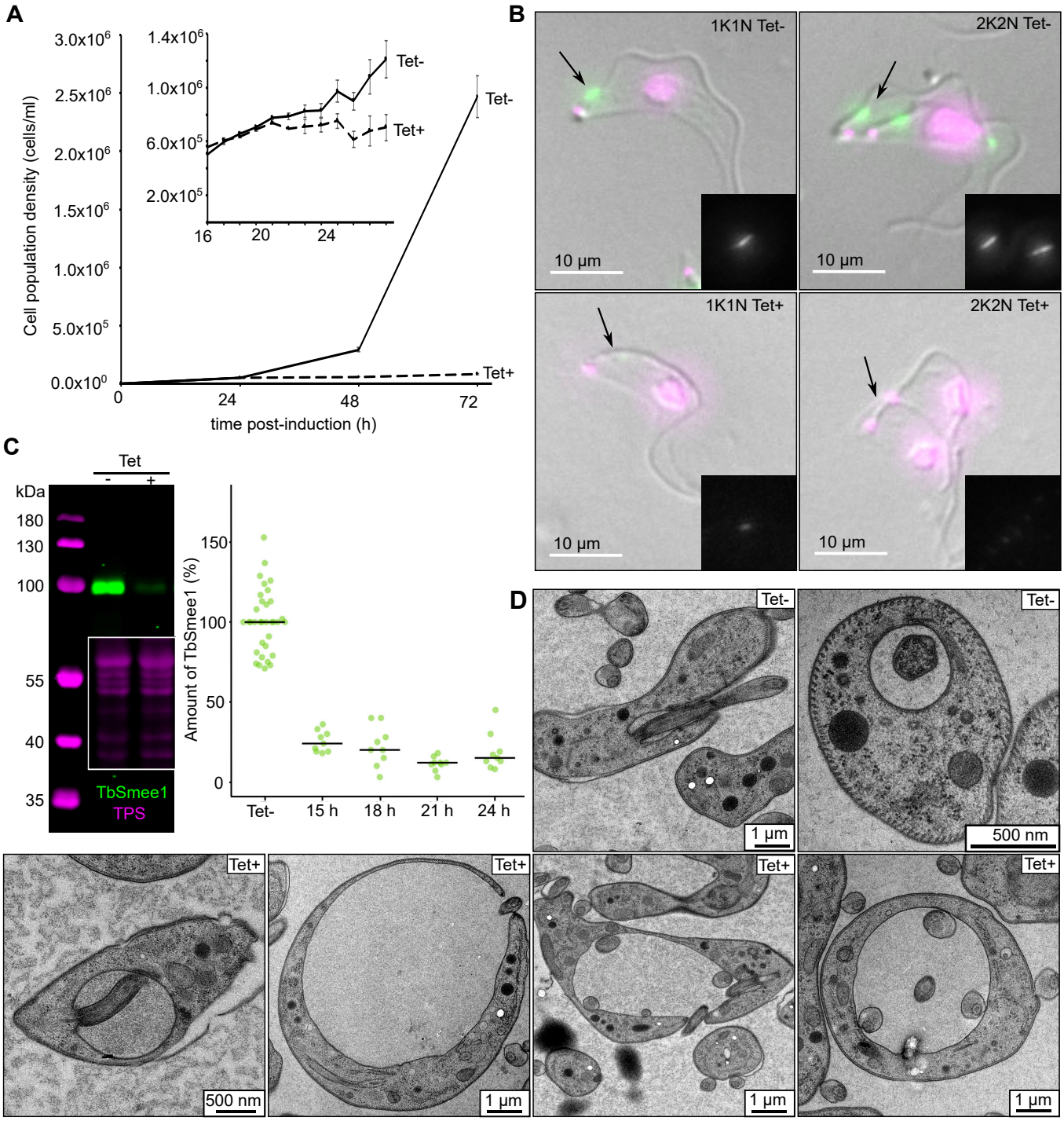

Figure 5. TbSmee1 is essential for the viability of bloodstream form T. brucei. (A) Depletion of TbSmee1 causes a strong growth defect. The population density of uninduced control (Tet-) and TbSmee1-depleted (Tet+) cells were measured at regular intervals after induction of RNAi over a 72 h timecourse. The insert shows data from a more high-resolution experiments with readings taken at hourly intervals. A growth defect was evident from 21 h post-induction onwards. (B) Confirmation of TbSmee1 depletion at the single-cell level. Uninduced control (Tet-) and TbSmee1-depleted (Tet+) RNAi cells were extracted, fixed, and labelled with anti-TbSmee1 antibodies (green). DNA was labelled with DAPI (magenta). Maximum intensity projections of the fluorescence channels are shown overlaid with a single DIC z-slice. Insets show the TbSmee1 signal. Exemplary 1K1N and 2K2N cells from each condition are shown. (C) Confirmation and quantification of TbSmee1 depletion. Whole-cell lysates from control (Tet-) and TbSmee1-depleted (Tet+) RNAi cells were immunoblotted using antibodies against TbSmee1 (green). Total protein stain (TPS, magenta) was used for signal normalisation. An exemplary immunoblot is shown. Normalised TbSmee1 signals in +Tet cells were expressed relative to the -Tet signal for each sample. TbSmee1 -Tet signals were expressed relative to the mean of all TbSmee1 -Tet values in the dataset. TbSmee1 depletion was quantified at the indicated timepoints post-induction. (D) Depletion of TbSmee1 results in an enlargement of the flagellar pocket. Electron microscopy images of control (Tet-) and TbSmee1-depleted (Tet+) RNAi cells are shown. The cells were fixed 24 h post-induction. All data in the

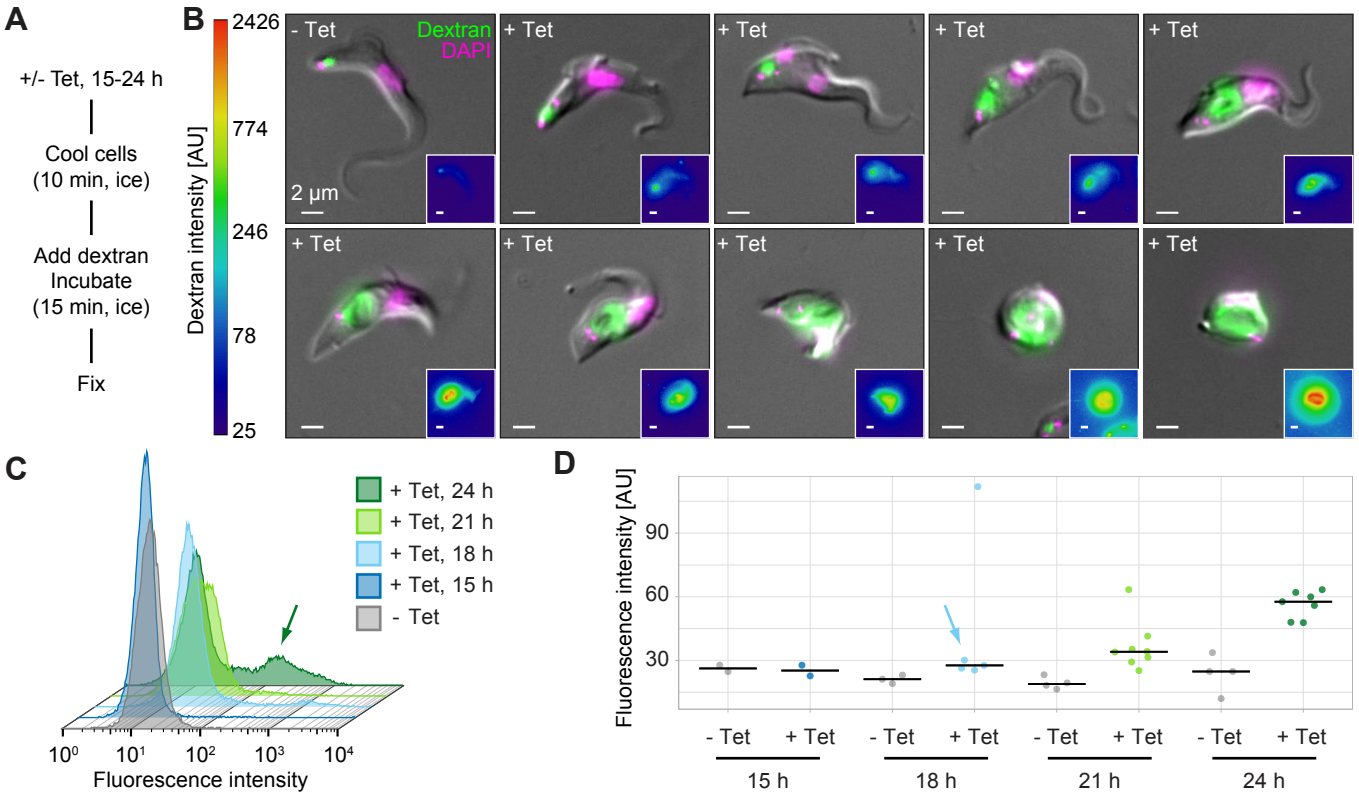

Figure 6. Flagellar pocket enlargement is an early consequence of TbSmee1 depletion. (A) Summary of dextran uptake protocol. The use of temperature blocks inhibits endocytosis, allowing dextran to enter the flagellar pocket but not be internalised. (B) The intensity of the dextran signal reports on flagellar pocket volume. Cells were incubated with fluorophore-conjugated dextran (green) prior to being fixed and imaged using fluorescence microscopy. DNA was labelled with DAPI (magenta). Exemplary cells from control (- Tet) and TbSmee1-depleted (+ Tet) conditions are shown. The + Tet cells exhibited various degrees of flagellar pocket enlargement and progressive morphological aberration. Insets show the dextran signal with a log-scale LUT. (C) Flow cytometry analysis of control (- Tet) and TbSmee1-depleted (+ Tet) cells incubated with fluorescent dextran at various timepoints after induction of RNAi. At later timepoints there is a clear emergence of a subpopulation of cells with much greater fluorescence intensity (arrow). Exemplary traces from a single experiment are shown. (D) Quantification of flow cytometry data. The geometric mean of the fluorescence intensity in control (- Tet) and TbSmee1-depleted (+ Tet) cells was measured at various timepoints after induction of RNAi. Bars indicate median values. The population mean of the + Tet cells was clearly higher at the later timepoints; a visible shift was visible as early as 18 h post-induction (arrow). All data in the experiments shown in this figure were obtained from multiple (n≥2) independent experiments; each experiment used three separate clones.

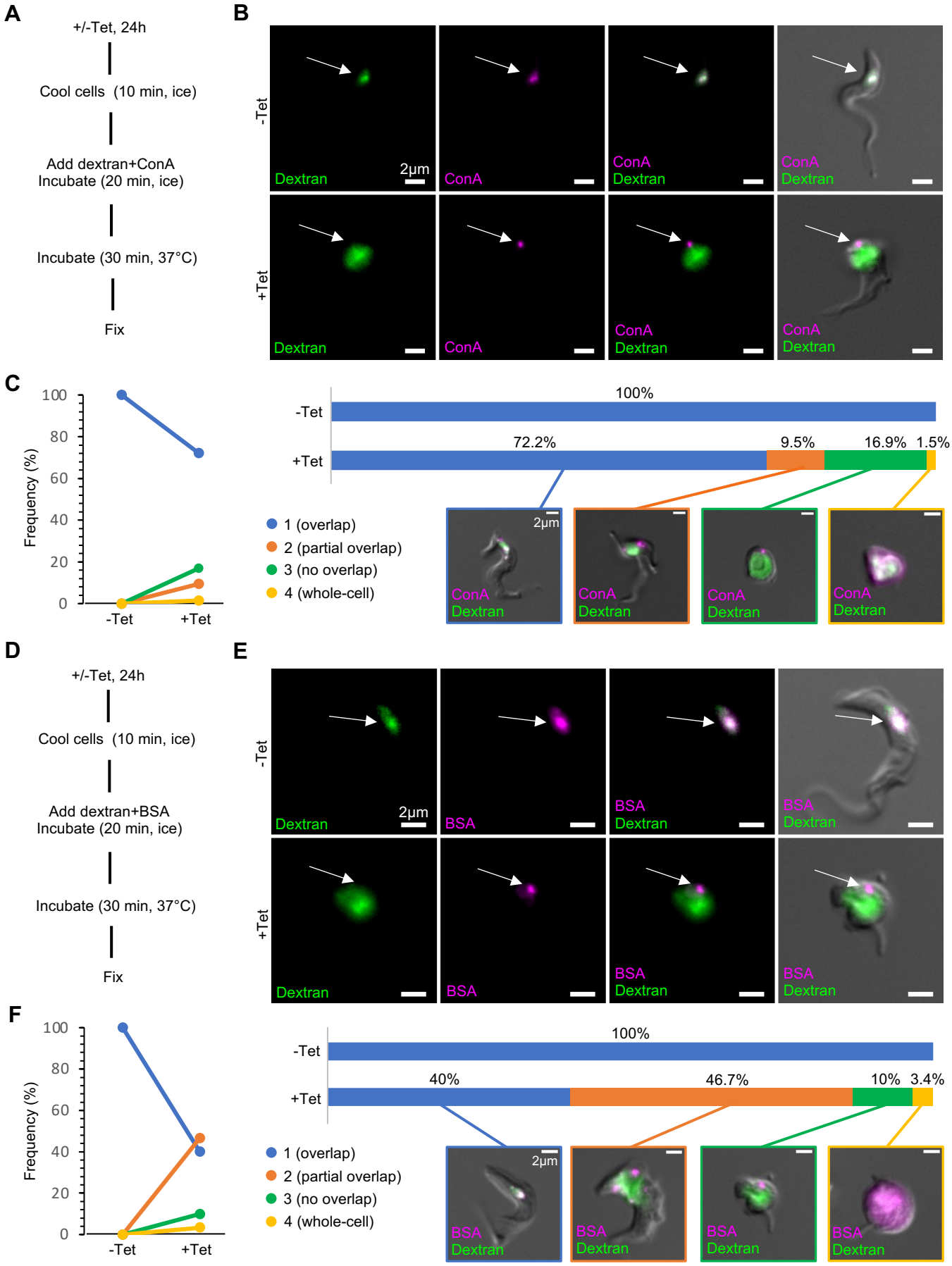

Figure 7. Surface-bound reporters cannot enter the flagellar pocket of TbSmee1-depleted cells. (A) Summary of paired dextran+ConA uptake protocol. (B) ConA is unable to enter the enlarged flagellar pocket of TbSmee1-depleted cells. In control (-Tet) cells, the dextran and ConA signals strongly overlapped (arrow, upper panels). In TbSmee1-depleted cells (+Tet), little to no overlap between the two reporters was observed (arrow, lower panels). Maximum intensity projections of the fluorescence channels are shown overlaid with a single DIC z-slice. (C) Quantification of dextran+ConA uptake experiments. Cells from control (-Tet) and TbSmee1-depleted (+Tet) samples were manually classified into four categories (1-4) based on the degree of overlap between the ConA and dextran reporters. Results are shown as a slope chart (left) and stacked bar chart (right); exemplary cells for each category are shown. (D) Summary of paired dextran+BSA uptake protocol. (E) BSA is unable to enter the enlarged flagellar pocket of TbSmee1-depleted cells. (F) Quantification of dextran+BSA uptake experiments. Data were obtained from multiple (n>3) independent experiments; each experiment used three separate clones.

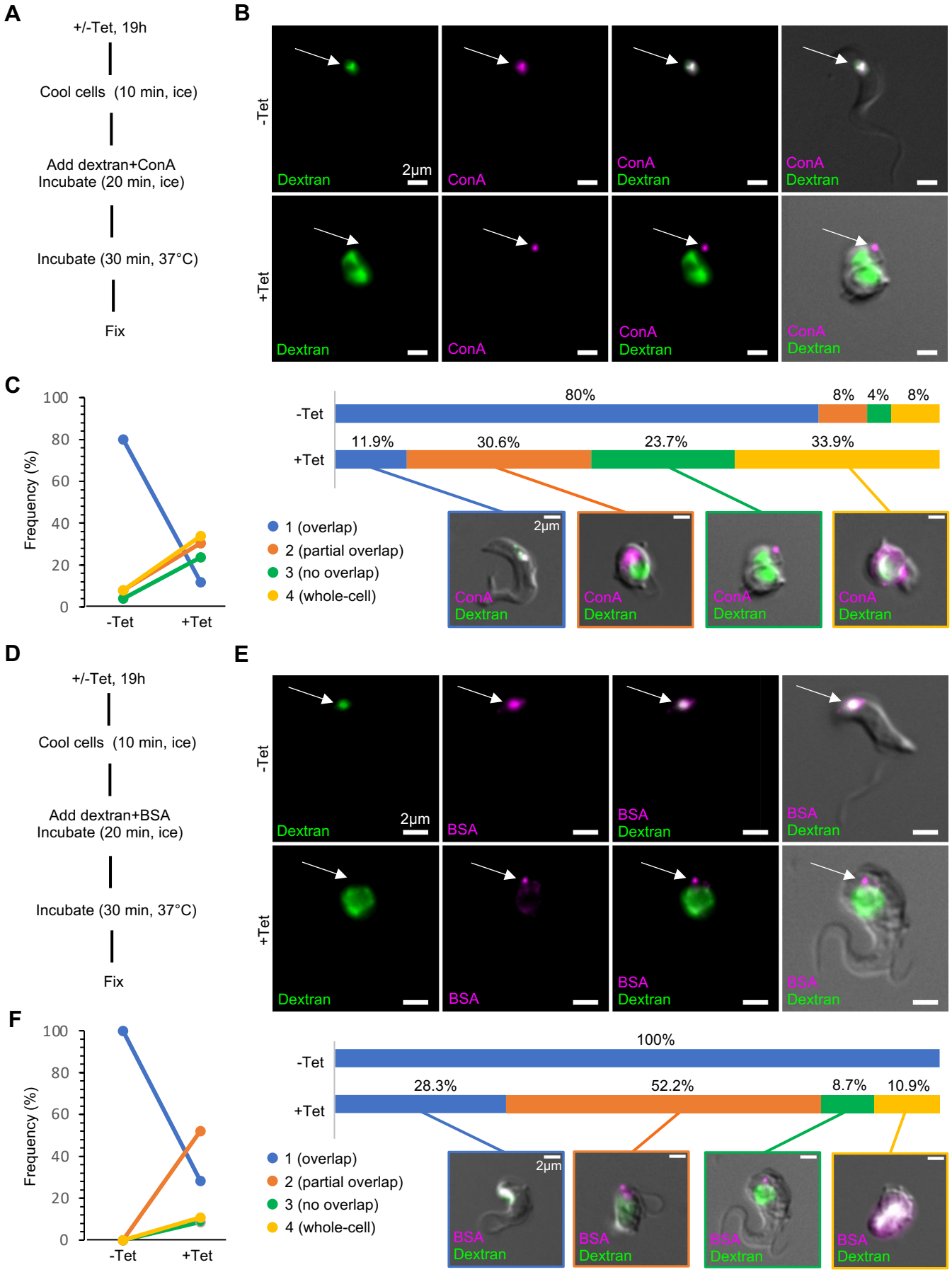

Figure 8. Blockade of surface reporters is due to an inhibition of endocytosis. (A) Summary of paired dextran+ConA uptake protocol. (B) ConA is unable to enter the enlarged flagellar pocket of clathrin-depleted cells. In control (-Tet) cells, the dextran and ConA signals strongly overlapped (arrow, upper panels). In clathrin-depleted cells (+Tet), little to no overlap between the two reporters was observed (arrow, lower-panels). Maximum intensity projections of the fluorescence channels are shown overlaid with a single DIC z-slice. (C) Quantification of dextran+ConA uptake experiments. Cells from control (-Tet) and clathrin-depleted (+Tet) samples were manually classified into four categories (1-4) based on the degree of overlap between the ConA and dextran reporters. Results are shown as a slope chart (left) and stacked bar chart (right); exemplary cells for each category are shown. (D) Summary of paired dextran+BSA uptake protocol. (E) BSA is unable to enter the enlarged flagellar pocket of clathrin-depleted cells. (F) Quantification of dextran+BSA uptake experiments. Data were obtained from multiple (n>3) independent experiments; each experiment used three separate clones.